AGU PUBLICATIONS

JGR

Journal of Geophysical Research: Solid Earth

RESEARCH ARTICLE
10.1002/2015JB012416

Key Points:
- Ridge to trench seismic reflection imaging across the Juan de Fuca plate
- Subduction bending faults extending to shallow mantle are imaged offshore Oregon
- Lower crustal ridgeward dipping reflections are observed in 6–8 Ma crust

Supporting Information:
- Figures S1 and S2
- Figure S3

Correspondence to:
S. Han,
han@ig.utexas.edu

Citation:
Han, S., S. M. Carbotte, J. P. Canales, M. R. Nedimović, H. Carton, J. C. Gibson, and G. W. Horning (2016), Seismic reflection imaging of the Juan de Fuca plate from ridge to trench: New constraints on the distribution of faulting and evolution of the crust prior to subduction, *J. Geophys. Res. Solid Earth*, *121*, 1849–1872, doi:10.1002/2015JB012416.

Received 3 AUG 2015
Accepted 24 FEB 2016
Accepted article online 29 FEB 2016
Published online 21 MAR 2016

Seismic reflection imaging of the Juan de Fuca plate from ridge to trench: New constraints on the distribution of faulting and evolution of the crust prior to subduction

Shuoshuo Han[1,2,3], Suzanne M. Carbotte[1], Juan Pablo Canales[4], Mladen R. Nedimović[1,5], Hélène Carton[1,6], James C. Gibson[1,2], and Greg W. Horning[4]

[1]Lamont-Doherty Earth Observatory, Palisades, New York, USA, [2]Department of Earth and Environmental Sciences, Columbia University, New York, New York, USA, [3]Now at Institute for Geophysics, University of Texas at Austin, Austin, Texas, USA, [4]Woods Hole Oceanographic Institution, Woods Hole, Massachusetts, USA, [5]Department of Earth Sciences, Dalhousie University, Halifax, Nova Scotia, Canada, [6]Institut de Physique du Globe de Paris, Paris, France

Abstract We present prestack time-migrated multichannel seismic images along two cross-plate transects from the Juan de Fuca (JdF) Ridge to the Cascadia deformation front (DF) offshore Oregon and Washington from which we characterize crustal structure, distribution and extent of faults across the plate interior as the crust ages and near the DF in response to subduction bending. Within the plate interior, we observe numerous small offset faults in the sediment section beginning 50–70 km from the ridge axis with sparse fault plane reflections confined to the upper crust. Plate bending due to sediment loading and subduction initiates at ~120–150 km and ~65–80 km seaward of the DF, respectively, and is accompanied by increase in sediment fault offsets and enhancement of deeper fault plane reflectivity. Most bend faulting deformation occurs within 40 km from the DF; on the Oregon transect, bright fault plane reflections that extend through the crust and 6–7 km into the mantle are observed. If attributed to serpentinization, ~0.12–0.92 wt % water within the uppermost 6 km of the mantle is estimated. On the Washington transect, bending faults are confined to the sediment section and upper-middle crust. The regional difference in subduction bend-faulting and potential hydration of the JdF plate is inconsistent with the spatial distribution of intermediate-depth intraslab seismicity at Cascadia. A series of distinctive, ridgeward dipping (20°–40°) lower crustal reflections are imaged in ~6–8 Ma crust along both transects and are interpreted as ductile shear zones formed within the ridge's accretionary zone in response to temporal variations in mantle upwelling, possibly associated with previously recognized plate reorganizations at 8.5 Ma and 5.9 Ma.

1. Introduction

At subduction zones, water stored and transported with the descending oceanic plate is gradually released at depth, strongly influencing the generation of earthquakes and arc magmatism [e.g., *Hacker et al.*, 2003; *Bangs et al.*, 2004; *Hyndman*, 2007; *Plank et al.*, 2013]. While thermally driven hydrothermal circulation can continue in the highly porous extrusive layer of the oceanic crust for millions of years after crust formation [e.g., *Grevemeyer and Weigel*, 1996; *Fisher et al.*, 2003], faults as local zones of high porosity and permeability constitute primary conduits for seawater to enter the deeper part of the crust and potentially the uppermost mantle [e.g., *Ranero et al.*, 2003; *Hayman and Karson*, 2009; *Shillington et al.*, 2015]. Thus, the distribution, geometry, and penetration depths of faults within the oceanic crust provide important constraints on the state of hydration of oceanic plates.

Faults in the oceanic plate first develop near the axis of mid-ocean ridges, contributing to the formation of the undulating ridge flank abyssal hill topography [*Carbotte and Macdonald*, 1994; *Macdonald et al.*, 1996]. At fast- and intermediate-spreading ridges, where most downgoing plates of the circum-Pacific subduction zones were formed, these faults are believed to be confined to the uppermost 2–3 km of the crust and cease growing within a few tens of kilometers from the ridge [e.g., *Macdonald et al.*, 1996; *Bohnenstiehl and Carbotte*, 2001]. In the vast plate interior, intraplate stresses are typically much smaller than the strength of the plate and little faulting is believed to occur [*Bergman*, 1986; *Wiens and Stein*, 1983]. Near the trench, the oceanic plate is flexurally bent due to subduction [e.g., *Watts*, 2001]. Here preexisting abyssal hill normal faults may be reactivated and/or new faults develop where bending stresses exceed the yield strength of the plate [*Billen et al.*, 2007]. Over the past decade, geophysical studies (mainly active source seismic studies) at different subduction zones have shown that these subduction bending-related faults may extend to the

uppermost mantle, providing pathways for fluids to reach beneath the crust and cause serpentinization of the mantle. [e.g., *Ranero et al*., 2003; *Ivandic et al*., 2008; *Tilmann et al*., 2008; *Lefeldt et al*., 2009; *Contreras-Reyes et al*., 2011; *Van Avendonk et al*., 2011; *Fujie et al*., 2013; *Shillington et al*., 2015]. Thus, a significant percentage of the total water carried into the subduction zone may be incorporated into downgoing plates within the outer trench slope region through subduction bend faulting.

At Cascadia, a young lithosphere end-member of the global subduction system, relatively little hydration of the downgoing Juan de Fuca (JdF) plate is expected due to its young age (~6–10 Ma at the subduction zone [*Wilson*, 2002]) and presumed warm thermal state [*Hyndman and Wang*, 1995]. However, numerous observations support the abundant presence of water within the subduction zone, including episodic tremor and slip (ETS) events possibly linked to fluid overpressures along the megathrust [e.g., *Rogers and Dragert*, 2003; *Audet et al*., 2009], reflection banding above the deep megathrust [e.g., *Hyndman*, 1988; *Nedimović et al*., 2003], reduced velocities within the mantle wedge [e.g., *Bostock et al*., 2002; *Brocher et al*., 2003], and the intermediate-depth earthquakes in the slab mantle beneath Puget Sound [*Parsons et al*., 1998; *Hacker et al*., 2003; *Preston et al*., 2003]. These observations suggest that the JdF plate is significantly hydrated as it enters the trench.

As an important constraint on plate hydration, the onset of plate bending and the distribution and extent of subduction bend faulting within the JdF plate is not well understood. The thick sediment cover above the oceanic crust fully buries the trench at Cascadia and prohibits direct identification of the basement fabric at the outer trench rise and slope. Moreover, unlike at many subduction zones, faults offsetting the seafloor in the outer trench slope are not observed in seafloor bathymetry [e.g., *Masson*, 1991; *Ranero et al*., 2003; *Fujie et al*., 2013; *Shillington et al*., 2015]. Early seismic studies at Cascadia are confined to the near-trench region (extending less than 50 km seaward of the deformation front) with the primary focus on the deformation of the accretionary prism [*MacKay et al*., 1992; *Tobin et al*., 1994; *MacKay*, 1995; *Moore et al*., 1995; *Flueh et al*., 1998; *Adam et al*., 2004; *Booth-Rea et al*., 2008]. The data acquisition configuration of these surveys (e.g., short streamer length, see summary in *Nedimović et al*., 2009) limited the ability of these studies to image the oceanic crust and uppermost mantle. On three seismic reflection lines collected in 2002 that extend ~150 km from the Juan de Fuca Ridge (JdFR), part way into the plate interior, *Nedimović et al*. [2009] observe vertical disruptions in the sediments indicative of active normal faulting beginning ~50–75 km east of the ridge axis, well beyond the crustal formation zone. By examining multichannel seismic (MCS) lines from eight previous surveys covering the near-trench area, *Nedimović et al*. [2009] identified larger offset normal faults in the sediments near the trench and inferred progressive growth faulting across the JdF plate. They interpreted the faulting as being caused by complex stresses within the JdF plate [*Wang et al*., 1997] with potential contributions from subduction plate bending, along with ridge and transform push, basal shear, and oblique subduction resistance. This study raised the possibility that a subduction bending-related faulting zone extends up to 200 km seaward from the deformation front, much wider than the region of plate bending expected for such a young and thin oceanic plate (for reference, the subduction bending region of the 30 Ma Nazca Plate at the Chile Trench at 38°S is ~150 km [*Contreras-Reyes and Osses*, 2010]). However, the data available for *Nedimović et al.'s* [2009] study were insufficient to distinguish between the relative contributions of subduction bending and contributions from other tectonic stresses to faulting within the sediment section and to determine whether there is evidence for bend faulting extending into the igneous crust and mantle near the deformation front. Moreover, except for the northernmost section of the Juan de Fuca plate, no prior seismic data were available from the central 50–250 km of the plate interior to link the lines of *Nedimović et al*. [2009] to the older profiles crossing the deformation front and to confirm the presence of faulting in the central region of the plate. How faulting patterns evolve across the aging JdF plate in response to flexural bending and other stresses in this tectonically complex region and how these faults may contribute to hydration of the plate prior to subduction were unknown.

In order to further our understanding of the evolution and hydration of the JdF plate prior to subduction, the JdF Ridge-to-Trench Experiment, a joint multichannel seismic (MCS) and wide-angle ocean bottom seismometer (OBS) survey were conducted during the summer of 2012 [*Carbotte et al*. [2012b], Figure 1]. This study provides plate-scale images and seismic velocity characterization of the sediments, crust, and shallowest mantle along two ridge-perpendicular transects offshore Oregon and Washington (hereinafter referred to as the Oregon and Washington transects). In addition, an ~400 km long trench-parallel line 10–15 km seaward of the Cascadia deformation front (along-strike transect) was acquired to characterize variations in plate structure along the margin. In this paper, we focus on the seismic reflection component of this experiment and present prestack time-migrated (PSTM) MCS reflection images of the two complete-plate transects from the JdFR to the

Cascadia deformation front. From these images, we characterize the crustal structure, distribution and extent of faults across the plate interior as the crust ages, identify where plate bending initiates, and determine the distribution and extent of faulting due to bending near the deformation front (Figures 2–8 and S3). The data reveal bright reflections from subduction bending faults transecting the crust and extending into the uppermost mantle offshore Oregon (Figures 2, 3, 6, and S3). Similar intracrustal and mantle fault plane reflections have only been observed previously offshore Nicaragua [*Ranero et al*., 2003] despite well-documented subduction bend faulting in many subduction zones [e.g., *Fujie et al*., 2013; *Shillington et al*., 2015]. The new data reveal different faulting patterns along the Oregon and Washington transects (Figures 2, 3, 6, 7, 9, and S3), with important implications for the state of hydration of the JdF Plate prior to subduction and the mechanisms of intermediate-depth intraslab earthquakes at Cascadia. In addition, a series of ridgeward dipping lower crustal reflections are imaged in 6–8 Ma crust on both transects (Figures 5 and 7), with characteristics similar to the events observed in old Pacific crust [e.g., *Ranero et al*., 1997b]. The implications of the new data for the origin of these distinctive lower crustal reflection events are discussed.

The results from other data of the JdF Ridge-to-Trench Experiment, including the MCS images of the continental slope and shelf along the Oregon and Washington transects and the along-strike transect [*Han et al*., 2013; *Han*, 2015], and the velocity structure derived from OBS data of these three transects [*Carton et al*., 2013; *Canales et al*., 2014; *Horning et al*., 2014; G. Horning et al., A 2-D Tomographic Model of the Juan de Fuca Plate from Accretion at Axial Seamount to Subduction at the Cascadia Margin from an Active Source OBS survey, *Journal of Geophysical Research*, in revision 2016], will be published elsewhere.

2. Geological Background

The Cascadia subduction zone extends along the west coast of North America, from northern California to British Columbia (~40°–51°N) (Figure 1). Here the oceanic JdF, Gorda, and Explorer plates subduct northeastward beneath the continental North America plate at a variable rate that increases northward from 30 to 45 mm/yr [*DeMets et al*., 2010]. The strike of the deformation front changes from almost N-S offshore northern California to NNW-SSE offshore Vancouver Island with an accretionary prism that is widest offshore Washington and narrows toward Oregon and Vancouver Island (Figure 1).

The subducting JdF plate is generated at the intermediate-spreading JdFR (half spreading rate ~28 mm/yr), which is currently subdivided into six spreading segments (Figure 1). During the past 17 Ma, the JdFR experienced seven major episodes of rift propagation, which left a series of prominent V-shaped propagator wakes within the plate interior, as is evident from offset magnetic anomalies (Figure 1) [*Wilson et al*., 1984; *Wilson*, 1993; *Wilson*, 2002]. These propagator wakes or pseudofault zones are believed to be more fractured than normal oceanic crust and represent localized weak zones in the plate [*Hey*, 1977]. Much of the JdF plate is covered by a thick sediment blanket due to the high abyssal plain sedimentation rate and deposits from the Astoria and Nitinat fans, which developed in response to deglaciation during the Pleistocene [*McNeill et al*., 2000; *Underwood et al*., 2005]. The close proximity of the Cascadia subduction zone to the JdFR results in a young plate age (~6–10 Ma) at the onset of subduction, with increasing crustal age to the south. The young age of the subducting plate, combined with the insulating effect of the thick sediment cover and the slow convergence rate, gives rise to a relatively warm subduction system [*Hyndman and Wang*, 1995].

Cascadia is an atypical subduction zone in that it generally lacks seismicity along the subduction plate boundary as recorded by onshore seismic networks [*Tréhu et al*., 2008; *McCrory et al*., 2012; *Tréhu et al*., 2015]. Although great ($M_w \sim =9$) megathrust earthquakes have occurred along this subduction zone in the geologic past, as evidenced from onshore and offshore stratigraphic records, no such megathrust earthquakes have occurred for the past $>$300 years [*Atwater and Hemphill-Haley*, 1997; *Goldfinger et al*., 2003]. Earthquakes in the overriding North America plate and the subducting JdF slab are also rare [*McCrory et al*., 2012; *Tréhu et al*., 2015]. Intraslab seismicity at Cascadia is sparse and shallow and occurs mainly in three areas: at 10–30 km depth beneath western Vancouver Island and northwestern California and at 30–50 km depth beneath Strait of Georgia-Puget Sound [*Kao et al*., 2008; *McCrory et al*., 2012; *Rogers and Crosson*, 2002]. Oregon has very few crustal earthquakes deeper than 30 km [*McCrory et al*., 2012; *Tréhu et al*., 2015]. Abundant episodic tremor and slip (ETS) is observed along the Cascadia subduction zone and exhibits notable spatial segmentation in periodicity [*Brudzinski and Allen*, 2007].

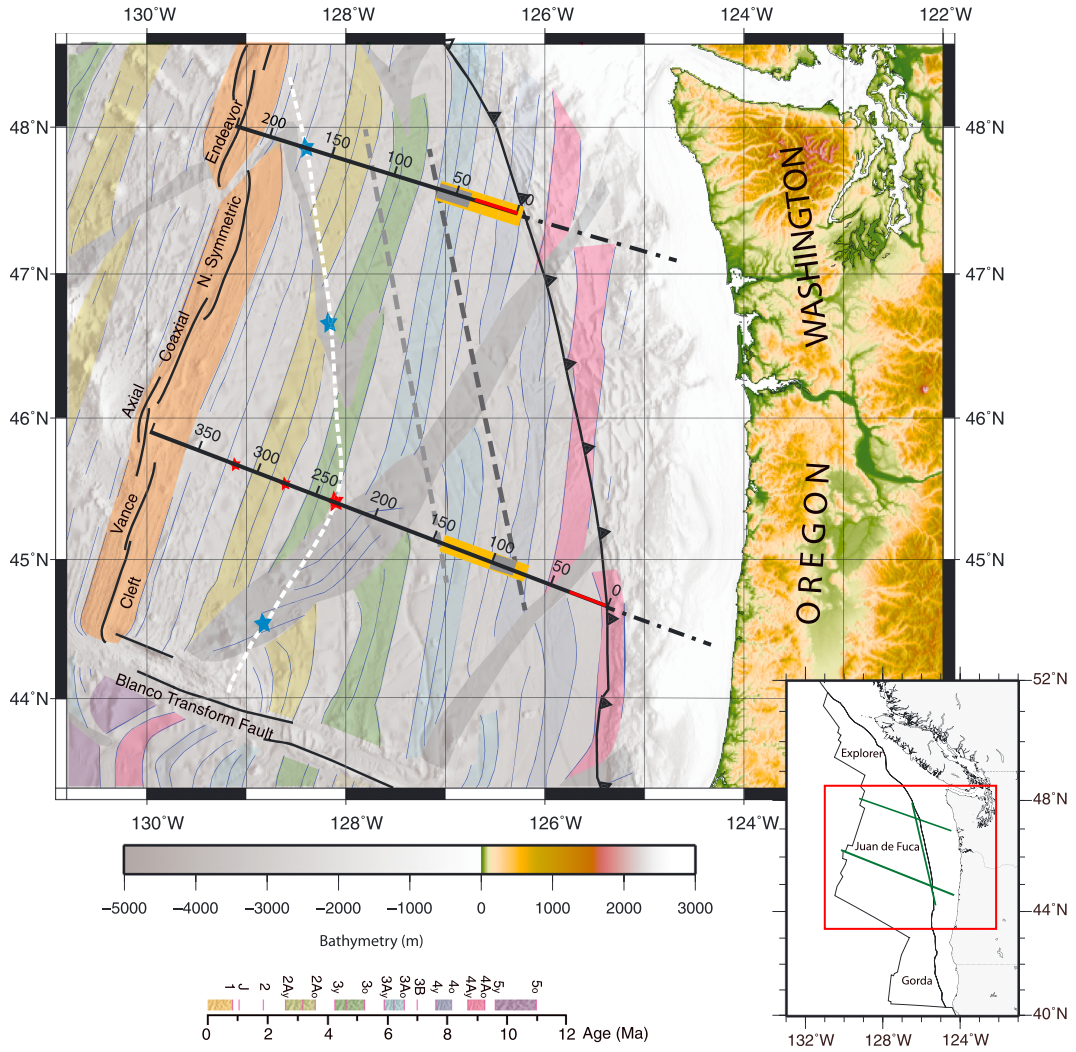

Figure 1. Regional map of the Juan de Fuca (JdF) plate and the Cascadia subduction zone offshore Washington and Oregon. Crustal age from *Wilson* [1993] shown as colored bands is superimposed over gray-scale bathymetry. Gray bands mark the propagator wakes. Juan de Fuca Ridge and Blanco transform fault are shown in thin black lines with ridge segments annotated. The deformation front (DF) of Cascadia subduction zone is in thin black line with thrust direction indicated. The thick black lines are the Oregon and Washington transections of the JdF Ridge-to-Trench Experiment; the seismic reflection images of the parts seaward of the DF (annotated ticks indicating distance in kilometers from the DF) are shown in this paper. Orange bars on both transects represent the distance range where the lower crustal ridgeward dipping reflections are imaged. Thin red bars near the deformation front show the distance range where bright fault plane reflections in the crust/mantle are imaged. Gray bars indicate locations of data gaps. White short dashed line on the plate outlines the seaward limit of normal faulting observed on the JdF plate with data constraints from *Nedimović et al.* [2009] (blue stars) and new constraints from this study (red stars). The big red star indicates the onset of extensive faulting in the plate interior, and the two small red stars show locations of the isolated faults further ridgeward. Light gray dashed line and dark gray dashed line show the initiation of plate bending due to sediment loading and subduction, respectively. Inset: regional map showing the locations of the Oregon transect, Washington transect, and along-strike transect of JdF Ridge-to-Trench Experiment.

3. MCS Data Acquisitions and Processing

The MCS data of the JdF Ridge-to-Trench Experiment were acquired aboard the *R/V Langseth* during survey MGL1211 [*Carbotte et al.*, 2012a, 2012b]. The sound source was a 6600 cubic inch air gun array towed at a nominal depth of 9 m and fired every 37.5 m. The data were recorded with an 8 km long solid-state streamer with 636 active hydrophones towed at a nominal depth of 9 m. The positions of sources and receivers were derived from GPS receivers located on the air gun source array and streamer tailbuoy and from the

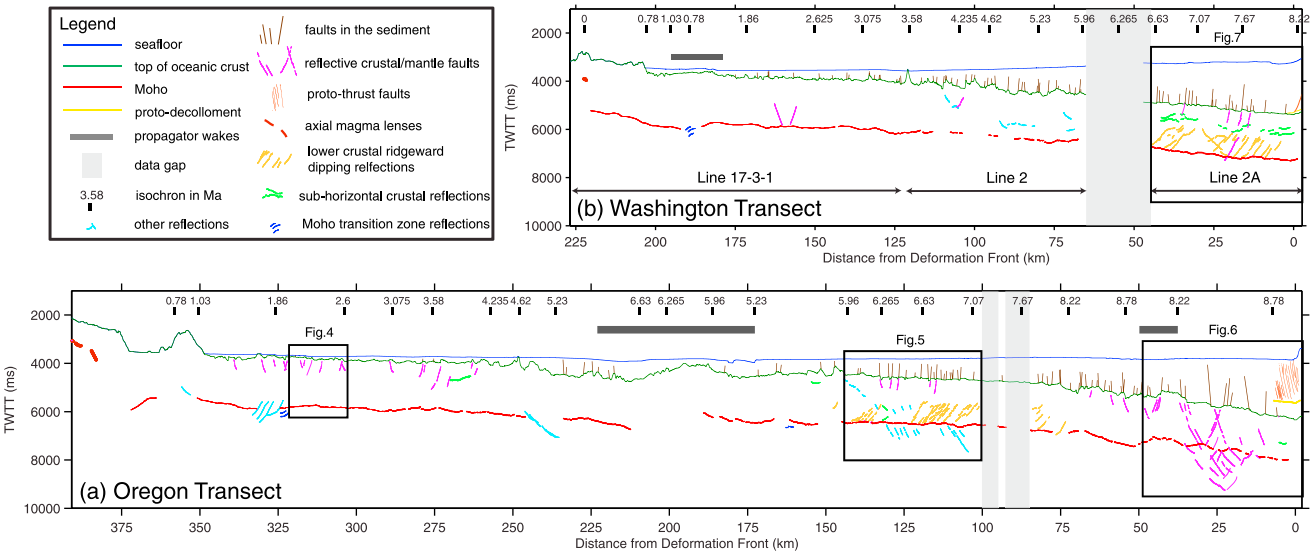

Figure 2. Interpretation of prestack time-migrated (PSTM) multichannel seismic (MCS) images of the (a) Oregon and (b) Washington transects. Features are annotated in the legend table. For Washington transect, Line 2A and Line 2 are data collected during survey MGL1211; Line 17-3-1 is from survey EW0207. MCS images of Line 17-3-1 from *Nedimović et al.* [2009] are used for the interpretation.

recordings of 26 compass-enhanced DigiCourse birds deployed along the streamer. Trace length is 12.28 s with a sampling interval of 2 ms.

The MCS data along the Oregon transect were acquired as one continuous profile (MCS Line 1), with the exception of two data gaps (~7 km and 5 km long, respectively) representing interruptions due to marine mammal mitigation (Figures 2, 3, and S3). The Washington transect consists of three parts: MCS Line 2A and Line 2 that were collected during survey MGL1211 and are separated by an ~20 km long data gap due to marine mammal mitigation and Line 17-3-1 collected during survey EW0207 and analyzed by *Nedimović et al.* [2009] following a somewhat different processing sequence (Figures 2, 3, and S3).

The MCS data were processed using the following sequence: a pseudo 3-D geometry was defined to minimize the effects of streamer feathering, with exact source-receiver offsets preserved and data binned into 6.25 m long common midpoint (CMP) gathers along track; band-pass filtering (3-7-220-250 Hz) was applied

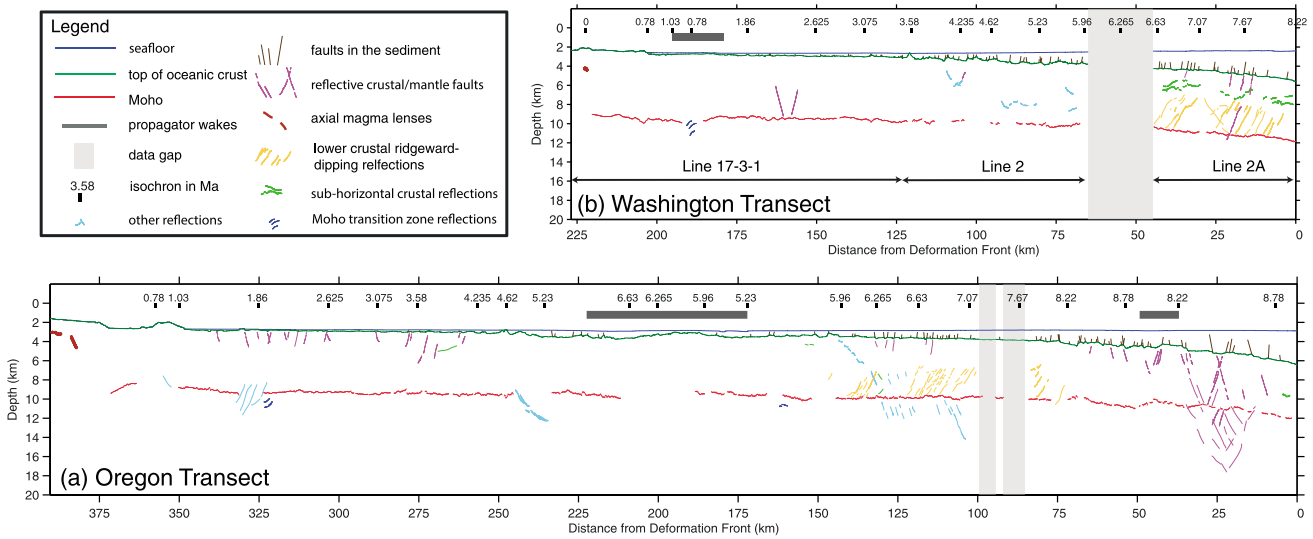

Figure 3. Interpretation of depth-converted PSTM images of the (a) Oregon and (b) Washington transects. Annotation is the same as in Figure 2.

to remove cable noise, followed by trace editing, spherical divergence correction, and resampling to 4 ms. Due to the electrical issues on board *Langseth* at the time of our survey, some channels are noisy with amplitude spikes. To enhance the signal-to-noise ratio and to avoid the smearing in later migration, despiking with the LIFT method [*Choo et al*., 2004] was applied (Figure S1). In our application of the LIFT method, the data were first divided into three frequency bands (low-frequency band: 0–14 Hz, midfrequency band: 14–56 Hz, and high-frequency band: 56–125 Hz). Despiking parameters (window and threshold of median amplitude filter) were determined for each individual frequency band and then applied to separate the data from each frequency band into signal and noise components. For the middle- and high-frequency bands, the residual signal was extracted from the noise component through an additional round of despiking based on coherency and amplitude criteria and was then added back to the signal component. Signals from the three frequency bands were finally combined to form the despiked shot gathers. This approach ensures good preservation of amplitude information [*Aghaei et al*., 2014; *Bécel et al*., 2015]. Along the portions of the two transects located just seaward of the deformation front, seafloor multiples arrive earlier than the Moho reflection and also obscure part of the lower oceanic crust. To address this issue, parabolic Radon filtering was applied to remove the seafloor multiple, also aiding in suppression of noise from side scattering. Predictive deconvolution was applied to collapse the air gun source bubble pulse reverberations. Detailed velocity analyses using the semblance method were conducted on supergathers at 100 CMP intervals (0.625 km) for the sediment section and crustal arrivals. A smoothed version of the resulting 2-D velocity function was used for prestack Kirchhoff time migration and was iteratively revised to yield optimal migration velocities and form the final prestack migrated images. From the migrated sections for both profiles, seafloor, top of basement, and Moho horizons, as well as intracrustal and mantle reflections, were identified and digitized with picking windows of 8 ms, 12 ms, 16 ms, and 20 ms, respectively (Figure 2). Locations of faults in the sediment section were determined from offsets in sediment layers. Local zones of reduced amplitude are observed that could be faint fault traces without resolvable offset but are not included in our interpretation.

The prestack time-migrated images were converted to depth using composite velocity models that combine smoothed sediment velocities derived from the MCS data and crustal and mantle velocities derived from the coincident OBS study along the Oregon transect [*Horning et al*., 2014; G. Horning et al., in revision, 2016]. Along the Oregon transect, *Horning et al*. [2014; in revision, 2016] derived a 2-D velocity model for the crust and upper mantle from a joint reflection-refraction traveltime inversion, from which they document velocity variations within the JdF plate from accretion to prior to subduction. For the Washington transect, where results from the coincident OBS study are not yet available, a 1-D crust-mantle velocity function (Figure S2) that corresponds with the average of the Oregon 2-D velocity model from 0 to 350 km from the deformation front (away from the JdFR) was used. The uncertainty of the sediment velocity is estimated to be less than 5%, and the uncertainty of the crust-mantle velocity model is in general $<=0.2$ km/s (G. Horning et al., in revision, 2016). Dips of crustal and mantle reflection events are measured from depth-converted sections; uncertainties vary with arrival time on the time section, velocity variations, and the approximation of possible curved fault surfaces by planar surfaces. The estimated uncertainties for upper crustal, lower crustal, and mantle events are ±3°, ±2°, and ±2°, respectively.

Using the one-eighth dominant wavelength criteria [*Widess*, 1973; *Cordsen et al*., 2000], the resolution of our reflection images permits identification of fault offsets of ~3–5 m at the seafloor and in the shallow sediments (dominant frequency 40–60 Hz, velocity 1.5–1.7 km/s), 4–13 m near the top of the oceanic crust (dominant frequency 35–55 Hz, velocity 1.7–3.5 km/s with the large velocity variation due to the variation of sediment thickness from near ridge to deformation front) and 28–90 m at Moho level (dominant frequency 10–30 Hz, velocity 6.6–7.2 m/s). Reflections from the fault planes in the oceanic crust and the mantle are imaged in our data. Assuming a given fault zone can be approximated as a thin layer embedded in constant velocity country rock [*Moore et al*., 1995; *Bangs et al*., 2009], fault zone widths need to exceed one-eighth of the dominant wavelength to be resolved, which corresponds to 10–60 m in the oceanic crust (dominant frequency 15–50 Hz, velocity 4.0–7.2 km/s) and 47–103 m in the uppermost mantle (dominant frequency 10–20 Hz, velocity 7.5–8.2 km/s) [*Widess*, 1973].

4. Results

In this section, PSTM images from the Oregon and Washington transects seaward of the Cascadia deformation front are presented. Results are described in terms of kilometer distance from the deformation front (at the toe of the accretionary prism) along our lines.

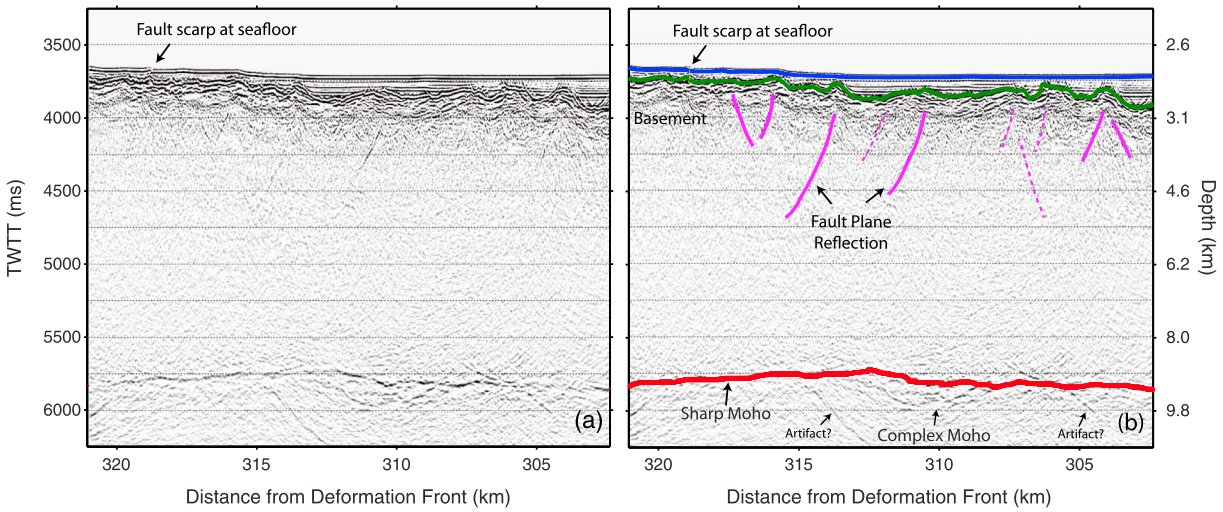

Figure 4. MCS (a) image and (b) interpretation illustrating the westernmost fault identified from the Oregon transect (offset at seafloor is marked) and the upper crustal dipping reflections attributed to alteration along preexisting abyssal hill fault planes in the plate interior. Relatively strong reflections are marked with solid lines, and relatively weak reflections are marked with dashed lines. Only the strong events are included in Figures 2 and 3. Moho with different reflection characteristics and two sub-Moho dipping events that may arise from overmigration of out-of-plane energy are annotated. Right-hand side labels are the approximate depths corresponding to the two-way traveltime labels on the left-hand side.

4.1. Oregon Transect

The Oregon transect spans ~390 km from Axial Volcano to the deformation front at ~44.6°N (Figures 2a, 3a, and S3a). Along this transect the oceanic plate is almost fully buried by sediments except for Axial Volcano and Son of Brown Bear Seamount located 35 km east of the JdFR axis [*Smith et al.*, 1994]. The sediment cover increases in thickness slowly from 0 to 310 ms two-way travel time (TWTT) (~300 m) within distance range 340–250 km, accumulates in the basin between 250 km and 180 km with maximum thickness of 850 ms (~830 m), and then thickens more rapidly trenchward due to sediment deposition from the Astoria fan and reaches ~2430 ms (~3490 m) at the deformation front (Figures 2a, 3a, and 8).

Beneath this sediment cover, the top of the oceanic crust dips gently toward the east with an angle of ~5° at the deformation front (Figure 3a). Superimposed on the regional eastward deepening trend are long-wavelength topographic undulations of the oceanic basement associated with a broad pseudofault zone crossed by this transect within distance range 172–222 km (Figures 1–3). This propagator wake encloses a block of 5.96–6.63 Ma old rotated oceanic crust and corresponds with a region of elevated basement bounded by deeper basement with a total relief up to ~730 ms (~740 m). Another pseudofault is crossed at distance 37–49 km and is associated with an ~8 km wide block lying at ~290 ms (360 m) higher than regional basement topography (Figures 2a, 3a, and S3a). In addition, the basement topography exhibits short-wavelength (~2–10 km) variations along the line that are presumably associated with the abyssal hills and small seamounts formed near the ridge axis. The short-wavelength basement relief is, in general, less than 500 m along the entire transect. Within distance range 75–140 km and 260–340 km, the basement is smooth with relief generally < 150 m, whereas within distance ranges 140–260 km and 0–75 km the basement is relatively rough (relief ~200–450 m) (Figures 2a, 3a, and S3a).

A Moho reflection is present along most of the profile with varying amplitude (Figures 2a, 3a, 4–6, 8, and S3). In the regions with smooth basement topography, Moho is strong and continuous, while at distance 140–260 km where basement topography is rough, Moho is a weak and diffuse reflection and is especially hard to image beneath the middle portion of the propagator wake. Near the deformation front, Moho is strongly reflective but discontinuous (Figure 6). Crustal TWTT over the whole transection is on average 1950 ± 120 ms (6160 ± 280 m) with a pronounced local increase in crustal TWTT near Axial Volcano (by 520 ms, Figures 2a and 8).

4.1.1. Faulting Within the Sediment Section

Faults within the sediment section are identified from near-vertical offsets in sediment layers. Within 5–6 km from the deformation front on the Oregon transect, a group of protothrust faults that dip trenchward and shoal into the protodecollement ~ 620 ms (~1.0 km) above the basement are imaged (Figures 2 and 6), which

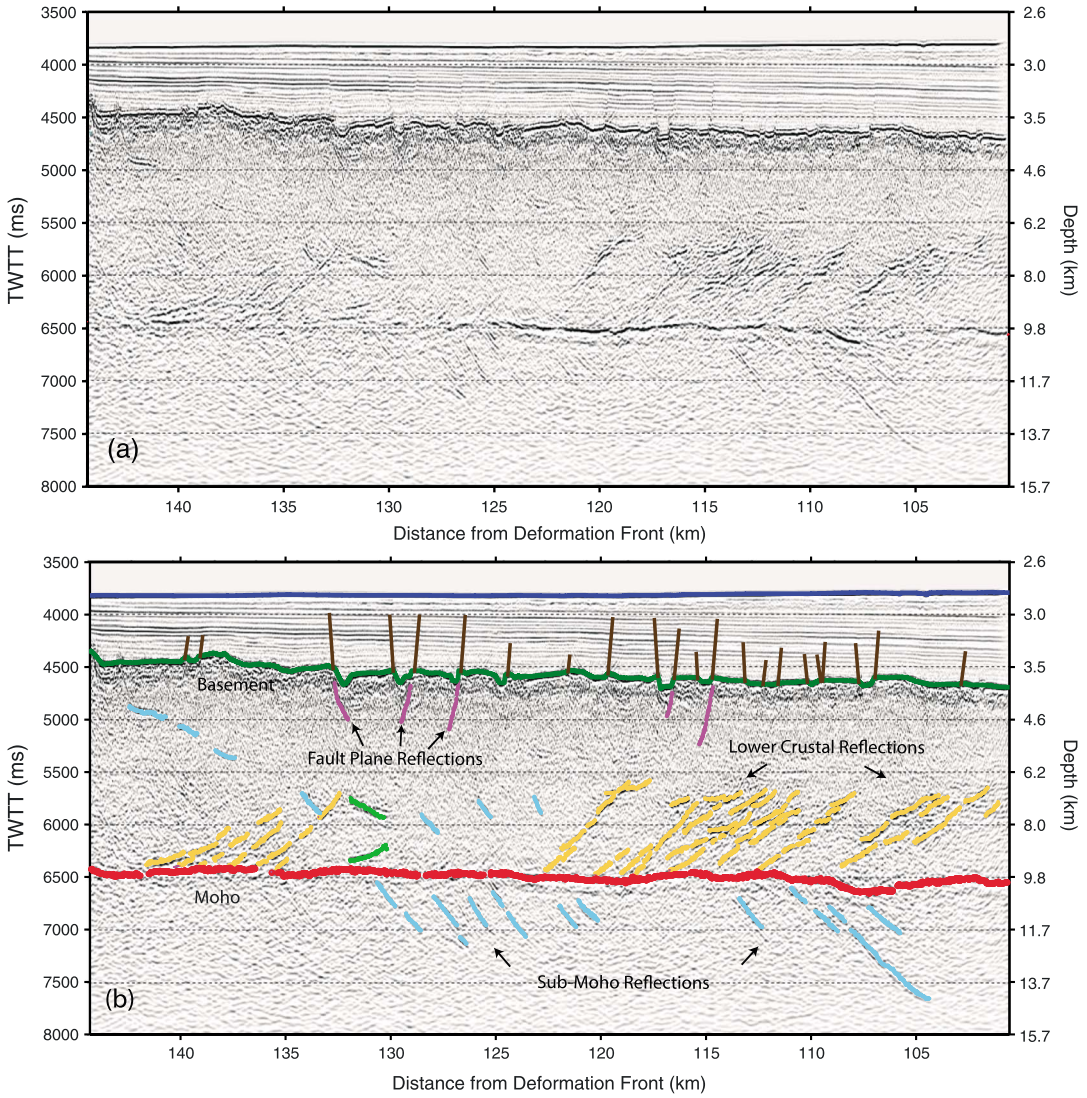

Figure 5. MCS (a) image and (b) interpretation of the portion of the Oregon transect with lower crustal ridgeward dipping reflections. Right-hand side labels are the approximate depths corresponding to the two-way traveltime labels on the left-hand side.

is similar to previous imaging [*MacKay et al*., 1992; *MacKay*, 1995]. All the other 76 faults identified in the sediment section along this transect display normal fault displacement. Ridgeward and trenchward dipping normal faults are observed in approximately equal numbers (Figure 9a). The westernmost fault is observed at distance 319 km (~70 km from the ridge axis) above 2.2 Ma crust and is associated with a vertical offset at the seafloor of ~12 m (Figure 4). Within distance range 130–320 km, faults are sparsely distributed (0–3 faults/10 km) (Figure 9a); most faults are observed in the sediment above the basement lows of the western propagator wake, and no faults are identified above the elevated basement block (Figures 2a and 3a). Fault density is $\geq$5 faults/10 km within distance range 40–130 km (except for the data gap zones) with a peak frequency of eight faults/10 km and is reduced within 40 km from the deformation front (Figure 9).

Most faults project to offsets in the oceanic basement, but the fault offset in the sediment section is generally smaller than the corresponding basement offset and decreases up section. Except for a few faults located around 230 km and a few others within 40 km from the deformation front, most faults terminate within the shallow sediment section; the shallow sediment above these faults appear undisrupted, within the limits of our vertical resolution of ~3–5 m (Figures 2a and 4). The upward decrease of fault offset is consistent with the characteristics of growth faults, and the near-basement offset represents the cumulative offset during the

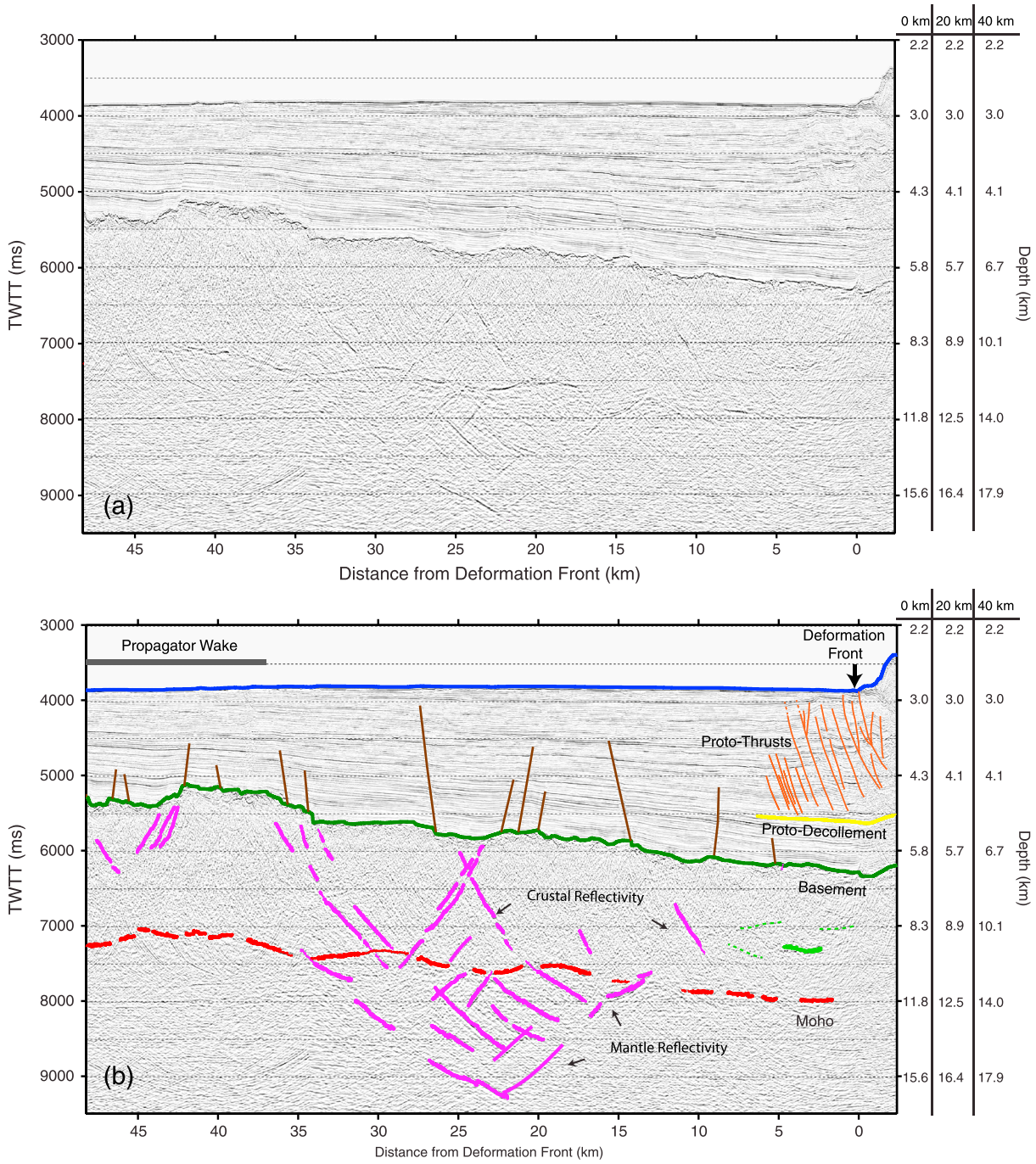

Figure 6. MCS (a) image and (b) interpretation of the near-trench portion of the Oregon transect (~45 km from deformation front). Relatively strong reflections are marked with solid lines, and relatively weak reflections are marked with dashed lines. Only the strong events are included in Figures 2 and 3. Right-hand side labels are the approximate depths corresponding to the two-way traveltime labels on the left-hand side. As the velocity varies rapidly in the horizontal direction near the deformation front, we give the approximate depths at 0 km, 20 km, and 40 km distance from the deformation front.

active period of the faults. We measure the fault offset from the deepest disrupted sediment layer that we can identify (generally within ~100 m from the basement) and calculate the average fault offset within 10 km bins along the profile to determine the general trend of fault offset variation across the plate (Figure 9). The average fault offsets are 6–15 m within distance range 150–320 km and 11–16 m within distance range 80–150 km and increase modestly to 24 m within distance range 40–80 km (Figure 9). Within 40 km from the deformation front, the average fault offset increases markedly with greater variability in offset (Figure 9).

The two faults with the largest offsets (100 m and 124 m) are trenchward dipping and extend close to the seafloor (Figures 6 and 9).

4.1.2. Reflectivity Within the Oceanic Crust

A variety of reflections are observed within the oceanic crust along the Oregon transect. Beneath Axial Volcano, two bright reflections are observed at ~970 ms and 1260 ms beneath the seafloor that correspond with the axial magma reservoir imaged by *Arnulf et al*. [2014]. Several weak dipping reflections with dip angles of 50–60° that extend from basement offsets downward into the upper crust are observed at distance 260–340 km (Figures 2a, 3a, and 4). Most of these reflections are confined to the uppermost 450–700 ms (~1100–1700 m in depth) of the crust (Figures 2a, 3a, and 4). Disruption in the sediment cover is only observed above one of these reflections. In addition, one subhorizontal reflection that is ~750 ms (~1880 m) beneath basement is imaged at distance 263–270 km. No intracrustal reflections are identified in the distance range spanning the western pseudofault (Figures 2a and 3a).

Within distance range 75–140 km, in the region of comparatively smooth basement, numerous small offset faults spaced ~1–2 km apart are observed that dip both ridgeward and trenchward and in places bound narrow, 70–120 ms (80–130 m) deep grabens (Figures 2a, 3a, and 5). The upper crust is weakly reflective with a few faint dipping (~50–65°) reflections imaged below basement offsets that can be connected to faults in the sediment section. In contrast, the lower crust shows abundant strong reflectivity with a series of prominent ridgeward dipping reflections (Figures 2a, 3a, and 5). These reflections begin ~1000–1100 ms (2900–3200 m) below the basement are spaced at 1–3 km and have dip angles of ~20°–40°. Each reflection event consists of several aligned short segments with varying reflection amplitude. Beneath these dipping reflections, Moho is a strong reflection at 1900 ± 65 ms (6180 ± 170 m) beneath basement (Figure 8), and, within our image resolution, there is no indication that Moho is offset by the ridgeward dipping lower crustal events (Figure 5). These events are notably absent from distance range 122–132 km, where a cluster of weak trenchward dipping reflections is observed. At distance range 132–140 km, a second group of ridgeward dipping events is imaged. They have similar characteristics as the first group but with diminished amplitude. Moreover, the Moho reflection beneath them is not as bright as below the first group of events (Figure 5).

In contrast to the rest of the Oregon transect, the oceanic crust imaged within 40 km from the Cascadia deformation front features several prominent reflections that transect both the upper and lower crust (Figures 2a, 3a, and 6). At the eastern edge of the elevated block associated with the easternmost propagator wake (distance 34–37 km), trenchward dipping reflections with dips of 50–60° are imaged in the upper crust and project to fault offsets in the sediments. Two of these reflections extend through the lower crust with dips of 40–45° near the Moho. Bright conjugate reflections are imaged beneath a basement graben centered at distance 25 km. Both reflection events project upward to faults in the sediment and can be traced down to disruptions in the Moho. Their dips are 50–55° within the crust, and they cross cut each other at ~400 ms (~900 m) beneath the basement. At distance 9–11 km, another bright trenchward dipping reflection (dip angle ~50°) is imaged 600–1300 ms (1820–3960 m) beneath the basement, which can be projected to a prominent fault in the sediment section.

4.1.3. Reflectivity Within the Uppermost Mantle

Along the length of our Oregon transect from the ridge axis to ~40 km from the deformation front, reflections beneath the Moho are rare (Figures 2a, 3a, and S3a). At distance range 323–333 km, a group of dipping events extending from the lowermost crust into the mantle is imaged. Next to these dipping events, a group of subhorizontal events are imaged to extend ~400 ms (~1.5 km) beneath the Moho at distance range 321–324 km. These events are similar to the sub-Moho events imaged elsewhere in this region, which have been interpreted as frozen magma lenses within a thick Moho transition zone [*Nedimović et al*., 2005]. Along the western edge of the western pseudofault zone (distance 235–246 km), a prominent trenchward dipping event is imaged that appears to extend from just above the Moho interface into the uppermost mantle by 780 ms (~3000 m). At distance 105–130 km, a group of faint trenchward dipping reflections are imaged, most of which are confined to 500–700 ms (1900–2700 m) beneath the Moho with one of them extending 1170 ms (~4500 m) into the mantle. Some of these events are located beneath the ridgeward dipping events imaged in the lower crust.

In contrast to the sparse and generally faint sub-Moho events in the plate interior, a series of bright mantle reflections are centered beneath the region of prominent through-going crustal reflections near the deformation front (14–34 km) (Figures 2a, 3a, and 6). These events are spaced ~2–4 km apart, dip either ridgeward or trenchward with ~35–50° dips, and extend up to 1600 ms (~6–7 km) beneath the Moho. The trenchward dipping events are more abundant, longer, and extend deeper than the ridgeward dipping ones. Some of

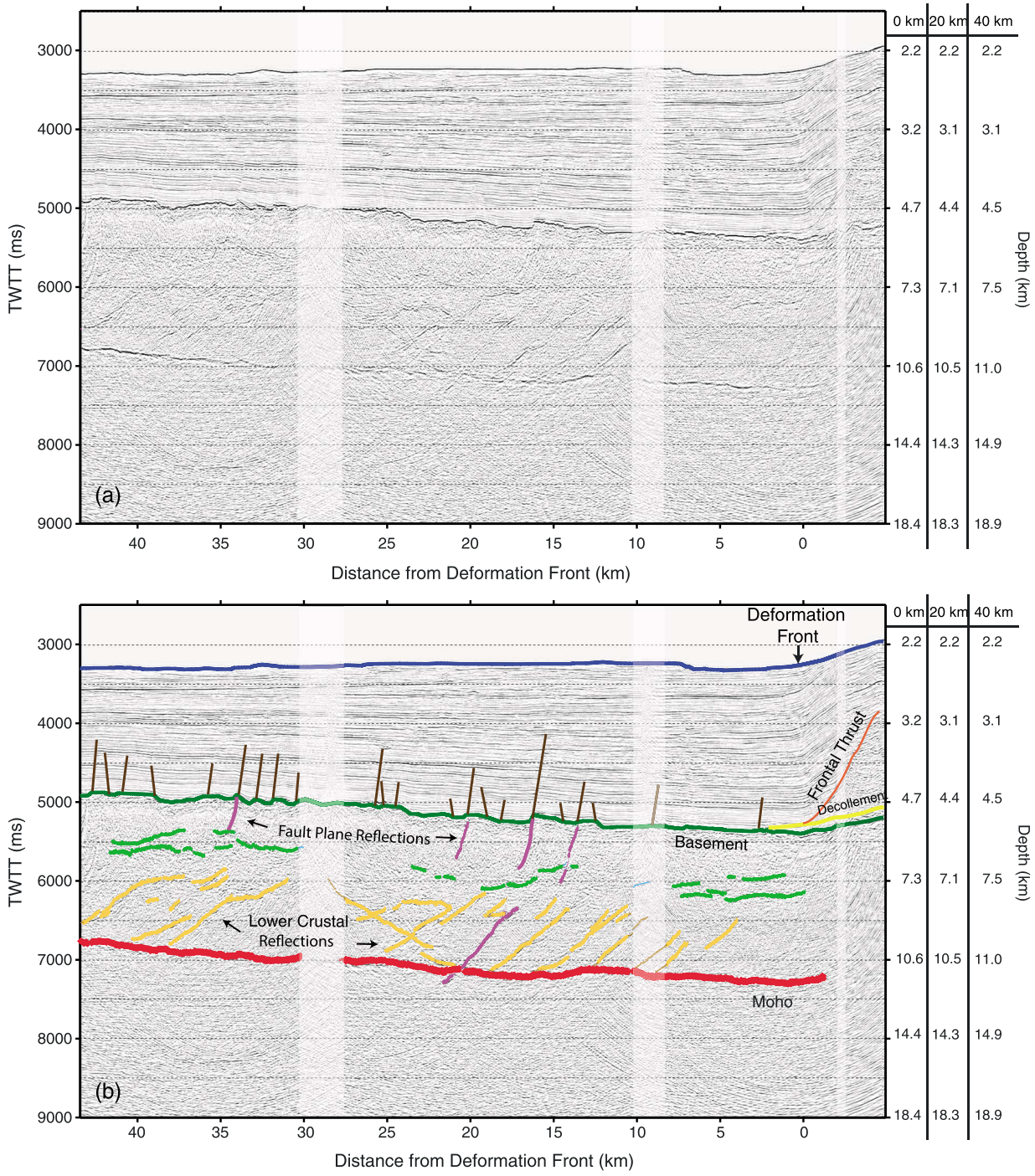

Figure 7. MCS (a) image and (b) interpretation of the near-trench portion of Washington transect (Line 2A, 45 km from deformation front). Three semitransparent vertical bars show locations of data gaps due to marine mammal mitigation. Right-hand side labels are the approximate depths corresponding to the two-way traveltime labels on the left-hand side. As the velocity varies rapidly in the horizontal direction near the deformation front, we give the approximate depths at 0 km, 20 km, and 40 km distance from the deformation front.

these mantle reflections connect with the crustal reflections. However, the density of events beneath the Moho is higher than in the crust above and they extend over a wider region than the crustal reflections. Within this distance range, a bright but discontinuous Moho is imaged that appears to be offset by these dipping events (Figure 6).

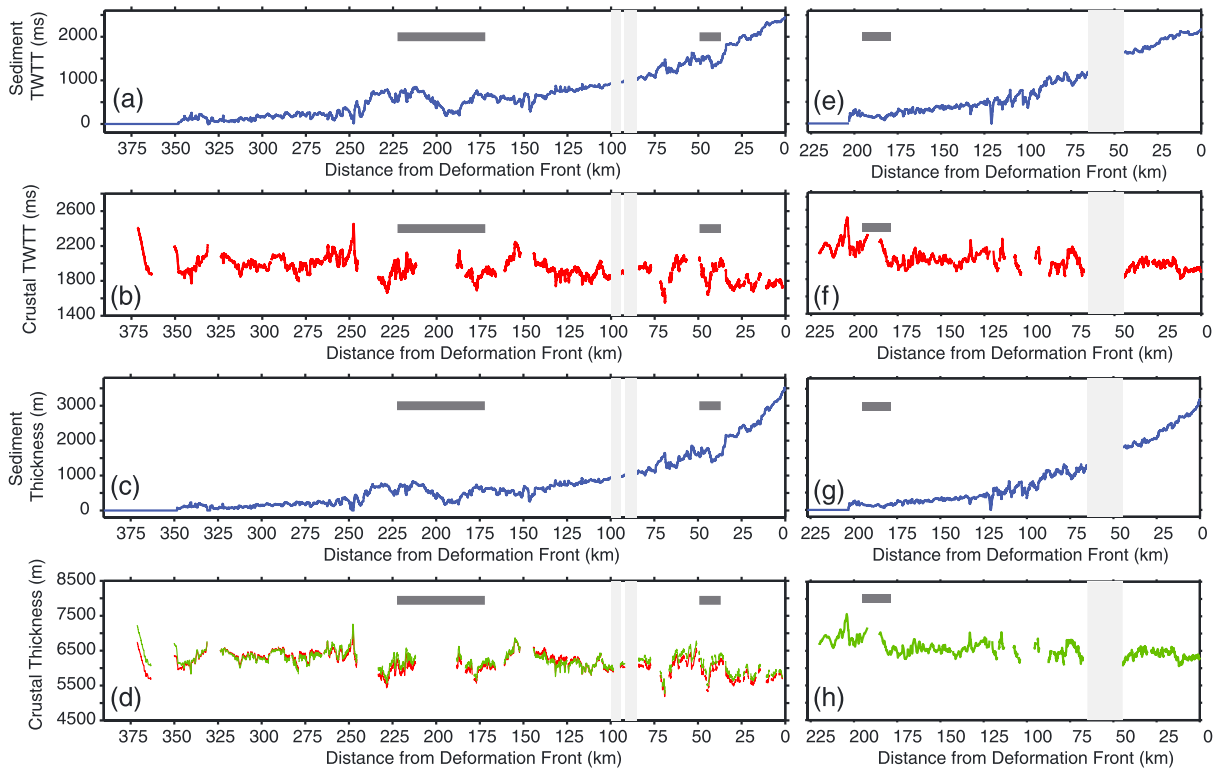

Figure 8. Sediment two-way traveltime (TWTT), crustal TWTT, and the depth-converted sediment thickness and crustal thickness along the (a–d) Oregon and (e–h) Washington transects. Dark gray horizontal bars show locations of propagator wakes. Pale gray vertical bars show location of data gaps. In Figure 8d, the red line shows crustal thickness result of depth conversion using G. Horning et al. (in revision, 2016) 2-D velocity model. In Figures 8d and 8h, the green lines show the crustal thickness result of depth conversion using a 1-D velocity function (Figure S2) averaged from distance 0–350 km of G. Horning et al. (in revision, 2016) 2-D velocity model. We acknowledge that the short-wavelength variation in crustal velocity that are caused by the variation of thickness and velocity of Layer 2A is not captured by the 2-D OBS velocity model used for the depth conversion. Therefore, the amplitude of the short-wavelength variation in our crustal thickness might be overestimated.

4.2. Washington Transect

The Washington transect extends ~222 km from the axis of the Endeavour segment of the JdFR to the Cascadia deformation front at ~47.4°N (Figures 2b and 3b). Along the length of this transect, oceanic crust is buried by hemipelagic sediments, basin turbidites, and the Nitinat fan deposits, except for a broad elevated plateau that spans the Endeavour ridge axis (~20 km half width) and a ~3 km wide, ~500 m high seamount that pierces the sediment cover at distance 122 km (Figures 2b and 3b). Sediment thickness increases trenchward from ~200 ms (~160 m) at distance 200 km, just east of the elevated plateau, to ~2170 ms (~3180 m) at the deformation front (Figures 2b, 3b, and 8).

Beneath the sediment cover, the top of the oceanic crust dips gently to the east, with the dip angle increasing to ~3° at the deformation front (Figure 2b). A local reversal in the dip of the oceanic basement is observed from distance 180–195 km where a propagator pseudofault zone is crossed and crustal age locally decreases to the east. Similar to the Oregon transect, the top of the oceanic crust shows variations in roughness with crustal age. The basement within distance ranges 125–180 km and 0–45 km is comparatively smooth with relief of less than 150 m, whereas the basement within distance range 65–125 km is relatively rough with ~250–500 m relief locally.

A Moho reflection can be identified along most of the Washington transect (Figures 2b, 3b, and S3b). It is a strong and continuous event beneath the regions of smooth basement topography and is weaker and more diffusive beneath the regions with rough basement topography (Figures 2b, 3b, and 7). The average crustal TWTT for the whole transection is 2040 ± 120 ms (6560 ± 240 m) (Figure 8).

4.2.1. Faulting in the Sediment Section

On the Washington transect near the deformation front, no trenchward dipping protothrust faults are observed. Rather, a ridgeward dipping frontal thrust—the first of a series of landward verging thrusts that dominate along this portion of the margin—is imaged and shoals into a decollement lying 60–80 ms (~120–180 m) above the

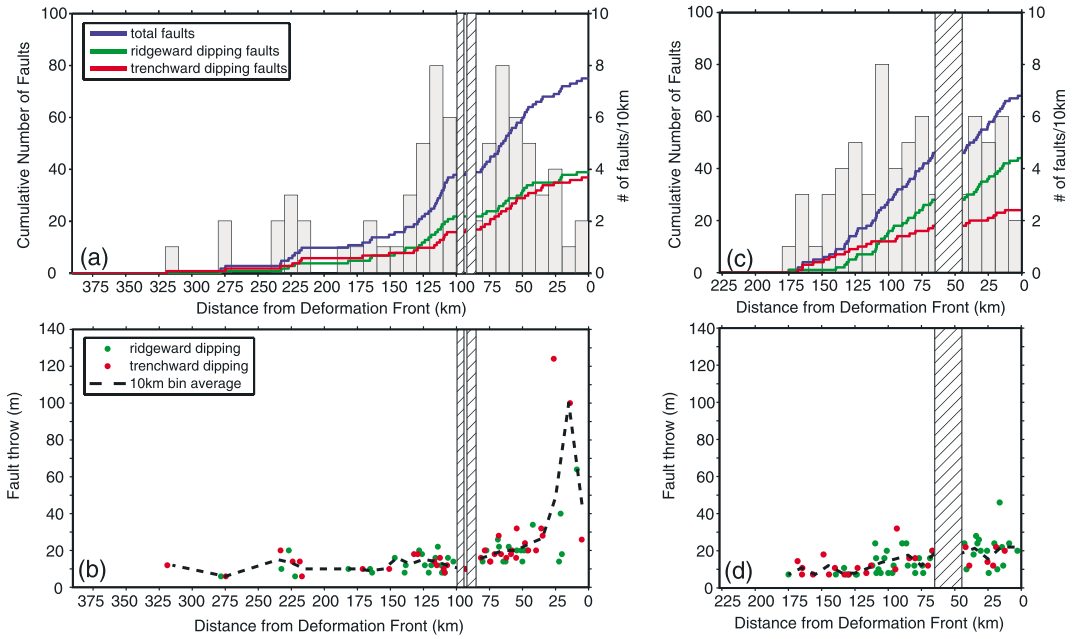

Figure 9. Faults detected in the sediment section along the (a and b) Oregon and (c and d) Washington transects. In Figures 9a and 9c blue, green, and red lines show cumulative number of all faults, ridgeward, and trenchward dipping faults, respectively, from the ridge axis to deformation front. Light gray bars show number of faults within 10 km bins along each profile. In Figures 9b and 9d fault offset measured from the lower sediment section near basement for ridgeward dipping faults (green) and trenchward dipping faults (red). Black dashed line shows average fault throw within 10 km bins. Hatched vertical bars show location of data gaps.

basement (Figures 2, 3, and 7). All the other 68 faults identified in the sediment section along this transect are normal faults. The westernmost imaged fault is located at distance 175 km, only ~50 km from the ridge axis, above ~1.66 Ma old crust (Figures 2 and 3). Fault density is 1–3 faults/10 km within distance range 180–130 km, is generally ≥5 faults/10 km within distance range 130–10 km (highest density is 8 faults/10 km, similar to that on Oregon transect), and is reduced to 2 faults/10 km closest to the deformation front (Figure 9). Two thirds of the faults dip toward the ridge, in contrast to the Oregon transect where trenchward and ridgeward dipping faults are present in roughly equal numbers (Figures 2, 3, and 9). Average fault vertical offset in the sediment above basement is 7–12 m within distance range 125–180 km, 8–19 m within distance range 65–125 km, and 16–22 m within distance range 0–45 km with the largest offset imaged by our data of 46 m (fault offset information is not available in the data gap between 45 and 65 km). Most faults can be traced into the sediments to less than ~1 km above the basement, including the faults closest to the deformation front.

4.2.2. Reflectivity in the Oceanic Crust

The western half of the Washington transect (distance range 125–225 km) corresponds with Line 17-3-1 of *Nedimović et al.* [2009]. The only intracrustal reflectivity observed along this line includes the 0.8 km wide axial magma lens imaged 1000 ms beneath the Endeavour ridge axis and a pair of lower crustal dipping reflections imaged at distance 160 km that are interpreted by *Nedimović et al.* [2009] as crustal faults (Figures 2b and 3b). No upper crustal dipping events comparable to those observed along the Oregon transect from distance 260–340 km are detected. However, it is noteworthy that the image of Line 17-3-1 was generated with a different processing sequence that was not optimized for resolving these dipping events. Thus, the scarcity of dipping reflection events could reflect differences in acquisition between the two surveys and/or processing. Within the new data from the Washington transect (east of distance 125 km), a few reflections are imaged in the upper crust within distance range 100–110 km, but only one may connect to a fault in the sediments above (Figures 2b and 3b). Sparse subhorizontal or dipping reflections are observed in the middle-to-lower crust within distance range 65–100 km, but none of them can be projected to an offset at the basement (Figuress 2 and 3).

Farther east, within 45 km from the deformation front, abundant reflectivity is found within ~6.63–8.22 Ma old crust (Figures 2b, 3b, and 7). The comparatively smooth basement in this region is offset by ridgeward dipping fault scarps <150 m high. Dipping upper crustal reflections are imaged beneath a few of the

basement steps. Except for one reflection event at distance 17 km that may extend through the entire crust to the Moho, most of these reflections only extend to 550–700 ms (~1400–1700 m) beneath basement. This depth extent is similar to that found for the upper crustal reflections observed at distance 75–140 km and 260–340 km on the Oregon transect. However, on the Washington transect, upper crustal reflections have somewhat steeper dips (60–65°) and are underlain by a group of subhorizontal reflections.

Within the lower crust in this region, a series of ridgeward dipping reflections are imaged in 6.63–8.22 Ma crust with similar characteristics to the lower crustal reflections observed in same age (~6–8.22 Ma) crust at distance range 75–140 km on the Oregon transect (Figures 2b, 3b, and 5). These events appear to initiate at about 1000–1100 ms (2900–3200 m) beneath the basement, are spaced at ~1–4 km, consistently dip toward the ridge, and merge into Moho with dips of ~20–40°. In this region, the Moho reflection is strong and continuous, without resolvable offsets coincident with the lower crustal reflections. It is noteworthy that these reflections cannot be traced to the upper crustal reflections and the upper and lower crustal events have different dip angles.

4.2.3. Reflectivity Within the Uppermost Mantle

Mantle reflectivity is absent along the Washington transect except for a cluster of sub-Moho reflections observed on the Line 17-3-1 portion of the transection (at distance ~190 km) and interpreted by *Nedimović et al*. [2005] as frozen magma lenses embedded within the Moho transition zone. Dipping events in the uppermost mantle, as observed along the Oregon transect beneath the ridgeward dipping lower crustal reflections, are not detected along the Washington transect.

5. Discussion

In the crustal sections along both profiles and in the mantle near the deformation front at the Oregon margin, we image dipping events that project or connect to basement fault scarps and faults in the overlying sediment section, providing strong evidence that these reflections arise from fault planes in the crust/mantle. In this section, we evaluate the potential contribution of subduction bending and sediment loading to the faulting observed offshore Oregon and Washington (section 5.1), discuss implications for hydration of the JdF plate prior to subduction at Cascadia (section 5.2), and address causes of the crustal and mantle fault reflectivity and the sources of water that percolate along the faults (section 5.3). In same age crust (~6–8 Ma) on both lines, we observe a group of ridgeward dipping lower crustal reflections (LCRs). These reflections do not connect to the upper crustal fault plane reflections, and shoal into the Moho reflection, arguing against them being crustal faults. We discuss the possible origins of these events in section 5.4.

5.1. Width of JdF Plate Bending Zone Prior to Subduction

On our MCS transects offshore Oregon and Washington, faulting in the sediment section begins 50–70 km from the axis of the JdFR (crustal age 1.7–2.2 Ma) and extends trenchward to the Cascadia deformation front with varying fault density (Figures 2, 3, and 9). This observation confirms the inference of *Nedimović et al*. [2009], based on their analysis of young crust and previously published near-trench data, of pervasive faulting in the interior of the JdF plate. These authors speculate that subduction bending along with other sources of oceanic plate stresses, including ridge and transform push, basal shear, and oblique subduction resistance [*Wang et al*., 1997], contribute to this pervasive faulting. Owing to the limited coverage of the available data, *Nedimović et al*. [2009] could not distinguish the subduction bending contribution from other potential factors. In this section, we estimate the location of the initiation of plate bending from basement topography along our two cross-plate transects, in order to determine the maximum width of the subduction bending region (Figure 10). Variations in the offsets of sediment faults and presence of crustal and mantle reflectivity along the transects indicate that active bend faulting of the JdF plate is occurring landward of the initiation of plate bending offshore both Oregon and Washington, with greater fault strain offshore Oregon.

Oceanic plate cooling with age, plate subsidence due to sediment loading, and plate bending due to subduction may all contribute to the gentle eastward dip of the oceanic crust toward the deformation front observed along both cross-plate transects (Figures 2 and 3). Subsidence due to plate cooling and sediment loading are estimated and removed from the basement topography as follows.

The plate cooling effect is calculated using a half-space cooling model [*Turcotte and Schubert*, 2002] (Figure 10).

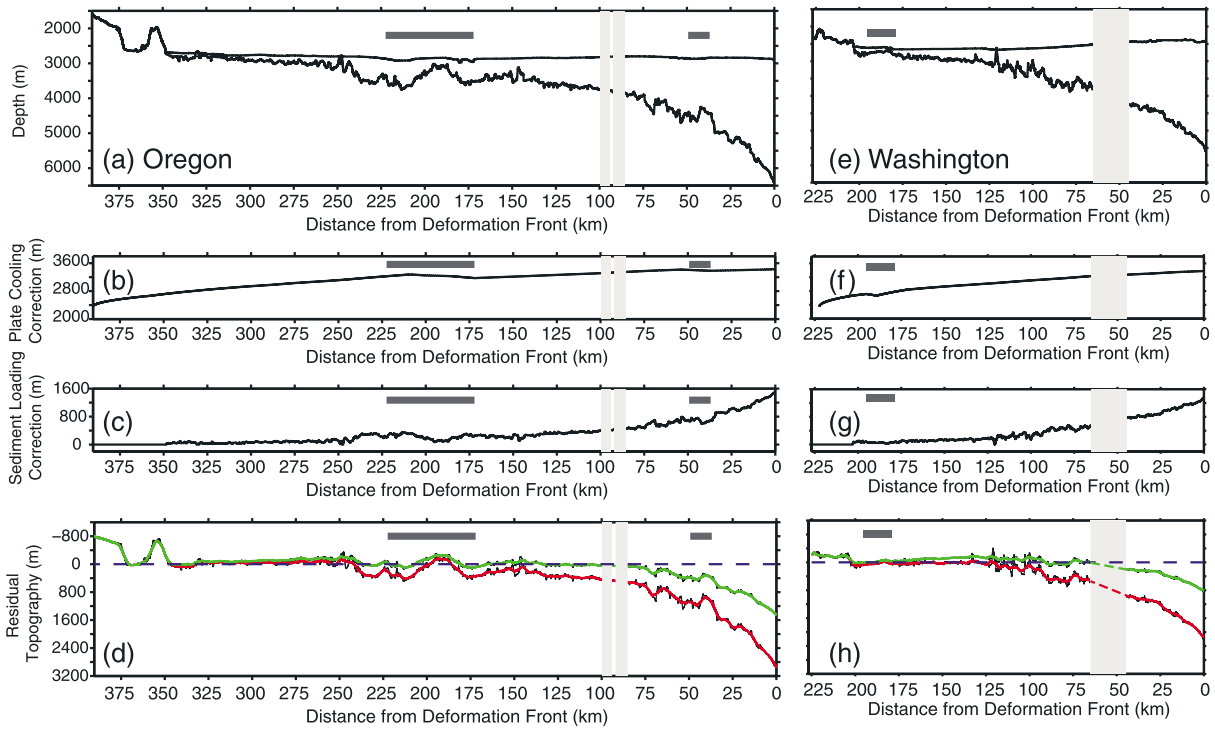

Figure 10. Estimation of the initiation of plate bending from basement topography along the (a–d) Oregon and (e–f) Washington transects. Plate cooling effect calculated using half-space cooling model (Figures 10b and 10f) and predicted subsidence due to sediment loading assuming local isostasy (Figures 10c and 10g) are removed from basement topography along the Oregon (Figure 10a) and Washington (Figure 10e) transects to determine the residual topography (Figures 10d and 10h). Bold red lines are the 5 km running average of the residual basement topography after removing the plate cooling effect. Bold green lines are the 5 km running average of the residual basement topography after removing both the plate cooling and the sediment loading effect. Blue dashed lines mark zero residual topography. Dark gray horizontal bars show locations of propagator wakes. Pale gray vertical bars show locations of data gaps.

$$z = z_0 + 360\sqrt{t} \tag{1}$$

where z is the depth to the top of the oceanic crust in meters predicted by half-space cooling, t is the age of the plate in Ma, and z_0 is the ridge axis depth. Here we use z_0 of 2350 m for both transects; this value is estimated from regional axial depths of JdFR, instead of the ridge axis depth of Axial Volcano and Endeavour segment, as these two segments are anomalously shallow due to the proximity of mantle melt anomalies associated with the Cobb Hotspot and Heckle seamount chain, respectively [*Karsten and Delaney*, 1989; *Carbotte et al.*, 2008]. In our calculations of oceanic crustal depth with plate age, we account for the age discontinuities along each transect associated with the propagator wakes (Figure 10). The thermal effect of sedimentation is not accounted for in the calculation.

Subsidence due to sediment loading is estimated assuming local isostasy [e.g., *Adam et al.*, 2005].

$$z_s = h_s \frac{(\rho_{\text{sed}} - \rho_{\text{water}})}{(\rho_{\text{mantle}} - \rho_{\text{water}})} \tag{2}$$

where z_s is basement subsidence resulting from sediment loading, h_s is sediment thickness, ρ_{sed}, ρ_{water}, and ρ_{mantle} are the sediment, seawater, and mantle rock density, respectively.

This approximation has been shown to be valid for young and thin plates with elastic thickness less than 20 km [*Contreras-Reyes and Osses*, 2010], which is appropriate for the JdF plate. Sediment thickness is obtained from depth-converted MCS images; seawater and mantle rock density of 1030 kg/m^3 and 3300 kg/m^3 are used, and a uniform sediment density of 2000 kg/m^3 is assumed for simplicity. Average sediment density is likely to vary along the profile due to the effects of sediment compaction, and we expect that our calculation overcorrects for sediment loading in younger, thinly sedimented crust (where the assumed sediment density may be too high), and undercorrects for sediment loading near the deformation front (where the assumed sediment density may be too low).

The predicted basement topography obtained from equations (1) and (2) is removed from the observed topography to obtain the residual topography shown in Figure 10. On the Oregon transect, the residual basement topography after removal of the plate cooling effect follows the zero line well for distance ranges 240–350 km. Aside from the anomalous topography associated with the wide propagator wake, the topography starts to systematically deviate from the zero line at 145–150 km. The residual topography after removal of both plate cooling and sediment loading effects follows the zero line well in distance range 210–240 km and 80–165 km. It lies slightly above the zero line in younger crust (distance range 240–350 km) due to overcorrection for sediment loading and in distance range 165–210 km associated with the wide propagator wake (Figure 10). The residual basement topography begins to deviate downward from the zero line at distance ~75–80 km from the deformation front which we attribute to the initiation of subduction bending. Similarly, from calculations of residual basement topography along the Washington transect, we infer that the initiation of bending due to sediment loading alone is at 120–125 km from the deformation front and to the combined effects of sediment loading and subduction at less than 65–70 km from the deformation front. The location of initiation of plate bending defines the maximum possible range for bending-related faulting to take place, as faults will only develop or be reactivated where bending stresses (related to the curvature of the downgoing plate) exceed the yield stress, which may not occur at the point of bending initiation.

Constraints on how the JdF plate deforms in response to plate bending are derived from variations in sediment fault offsets and the distribution of crustal and mantle reflectivity along our transects (Figures 6, 7, and 9). On the Oregon transect west of where plate bending initiates (distance range 150–320 km), average fault offsets range from 6 to 15 m with no resolvable increase with increasing crustal age. Within distance range 80–150 km where plate bends due to sediment loading, average fault offsets range from 11 to 16 m and do not show increasing trend. East of where the subduction bending initiates, the average fault offset increases modestly from 17 m to 24 m from distance 80 km to 40 km. Within 40 km from the deformation front, the average fault offset increases markedly with two trenchward dipping faults located at 24 km and 15 km, respectively, reaching offsets of 124 m and 100 m and displaying resolvable fault offset near the seafloor. Within this region where the largest sediment fault offsets are found, bright fault plane reflections are observed in the crust, some of which offset Moho, along with a group of prominent mantle reflections that extend to 6–7 km below Moho. No similar reflections cutting across the crust are observed farther in the plate interior on this profile. We interpret the fault slip within 80 km from the deformation front along the Oregon transect as due to subduction bending, with faults within 40 km from the deformation front accommodating the majority of bending deformation. In comparison, along the Washington transect, the average fault offsets are in a narrow range (7–12 m) west of 125 km where the plate bending initiates but increases from 8 m to 19 m within distance range 125–65 km where the plate bends due to sediment loading. A modest further increase in average fault offsets occurs within 45 km of the deformation front (19–22 m), with a maximum fault offset of 46 m. There is no detectable disruption of the sediment section shallower than ~1 km above basement in this region. In the oceanic crust, several fault plane reflections are observed within the middle-to-upper crust beneath basement fault scarps, including the fault associated with largest offset in the sediment (Figure 7), but they do not cut across the Moho. No mantle reflections are observed. Our data support limited bend faulting within 70 km from deformation front along the Washington transect, although the possibility that the upper crustal reflectivity and small increase in sediment fault offset reflect the accumulated strain under plate interior stresses cannot be ruled out.

In summary, based on our estimation of the location of the onset of plate bending and analysis of fault characteristics and crustal/mantle reflectivity, we conclude that the JdF plate starts to bend due to sediment loading at ~120–150 km seaward from the deformation front and due to the combined effect of sediment loading and subduction at ~65–80 km seaward from the deformation front. Most of the bend faulting deformation occurs within 40 km from the deformation front, as evidenced by the increase in sediment fault offsets and the enhancement of deeper fault reflectivity. Other mechanisms such as complex intraplate stresses [*Wang et al.*, 1997] and/or differential compaction [*Gibson et al.*, 2014] are needed to account for faulting observed within the sediment section further seaward in the plate interior (>120–150 km from the deformation front).

5.2. Causes of Different Faulting Patterns Offshore Oregon and Washington and Implications for Plate Hydration Prior to Subduction

Our MCS data reveal more extensive and deeper penetrating subduction bend faults offshore Oregon than Washington, and therefore, greater hydration of the plate in this region near the deformation front is inferred.

What causes the different bend faulting patterns at the Cascadia margin offshore Oregon and Washington? Differences in plate bending stresses due to differences in the downdip curvature of the JdF plate may play an important role. Due to change in orientation of the deformation front from Oregon to Vancouver Island, the slab is arch shaped beneath northern Washington, with a shallower (10°) slab dip in this region observed to a depth of about 50 km [*Creager et al*., 2002], whereas steeper dips are observed beneath Vancouver Island (~18° at 40–60 km depth) [*Davis and Hyndman*, 1989] and beneath central Oregon (~16° at 30 km depth) [*Gerdom et al*., 2000]. Given the shallower slab dip beneath Washington, plate bending stresses may be insufficient to induce significant deformation in the outer trench region. Another contributing factor may be differences in the orientation of the preexisting oceanic crustal fabric. Previous studies at a number of subduction zones, including Alaska, Middle America, Japan, and Chile, have found that where the strike of abyssal hill normal faults are at low angle (<25–30°) to the strike of the trench, these faults tend to be reactivated in response to plate bending rather than new faults forming [*Masson*, 1991; *Nakanishi*, 2011; *Ranero et al*., 2005]. Along the margin in the vicinity of our Oregon transect, the strike of the abyssal hill fabric inferred from magnetic isochrons (Figure 1) is nearly parallel to the trench, while inherited fault orientations are more oblique to the trench (~30°) where crossed by our Washington transect. Thus, abyssal hill faults offshore Oregon are expected to be more easily reactivated to accommodate bending-related deformation than along Washington.

The contrast in extent of bend faulting at the two margins has important implications for plate hydration prior to subduction, and the generation of intermediate-depth intraslab earthquakes at Cascadia. The origin of intermediate-depth (50–300 km) intraslab earthquakes is not well understood, as brittle deformation is not expected at these depths. One proposed mechanism invokes metamorphic dehydration which leads to elevated pore fluid pressures and weakening in the slab, facilitating brittle deformation [*Kirby et al*., 1996; *Hacker et al*., 2003]. At the Chile, Middle America, and Alaska margins, the density of outer trench slope bending-related faults is correlated with the abundance of intermediate-depth intraslab earthquakes further landward, supporting the hypothesis that the extent of alteration and plate hydration through outer-rise bend faulting plays an important role in intraplate seismicity [*Ranero et al*., 2005; *Shillington et al*., 2015]. At Cascadia the extent of subduction bend faulting is limited compared with these other margins and limited plate hydration presumably contributes to the low levels of intraplate seismicity observed [*Nedimović et al*., 2009]. However, the regional distribution of the intraslab seismicity that is observed, which is concentrated beneath Puget Sound in Washington and negligible beneath Oregon [*Wada et al*., 2010; *McCrory et al*., 2012], is inconsistent with the differences in subduction bend faulting along the margin.

The lack of intraslab earthquakes between 42° and 47°N was previously attributed to an anhydrous slab beneath Oregon [*McCrory et al*., 2012]. Our images of deep-penetrating, reflective fault zones near the deformation front offshore Oregon indicate that there is potential for water reaching at least 6–7 km into the mantle along fault zones, arguing against this hypothesis. Comparison of intraslab earthquake locations and slab images derived from receiver function and wide-angle reflection data shows that most of the Washington intraslab earthquakes are located near or within 10 km beneath the Moho of the downgoing plate [*Preston et al*., 2003; *Abers et al*., 2009, 2013] and this seismicity has been attributed to dehydration embrittlement in the serpentine or chlorite-bearing mantle [*Hacker et al*., 2003; *Preston et al*., 2003; *Abers et al*., 2013]. Our MCS image offshore Washington shows that most faults are confined to the upper-to-middle crust, suggesting that plate hydration prior to subduction is limited in this region and largely confined to the crust. Our data do not rule out ongoing hydration of the plate beneath the forearc due to continued bend faulting, as proposed in the recent numerical modeling study of *Faccenda et al*. [2009]. However, increased bend faulting and fluid circulation would also be expected beneath the Oregon forearc via this mechanism. As intraslab seismicity beneath Washington is most prevalent where the plate is warped, it has been suggested that slab flexure, in addition to the expected metamorphic dehydration, gives rise to enhanced seismicity [e.g., *Crosson and Owens*, 1987; *McCrory et al*., 2012]. Along with plate flexure, regional differences in the stress state of the downgoing plate associated with slab pull and mantle resistance forces as proposed by *Wada et al*. [2010] may also contribute to the regional differences in intraplate seismicity.

5.3. Reflectivity of Subduction Bending Faults in the Crust and Mantle

Our data reveal bright reflections from subduction bending-related faults transecting the oceanic crust and penetrating into the uppermost mantle along the Oregon transect and from upper to middle crustal faults near the deformation front on the Washington transect. Considering the small offsets of these faults

(less than 200 m at the basement), the expected impedance contrast between the basaltic/gabbroic rocks of the hanging wall and footwall is not sufficient to account for the observed reflectivity. To generate the observed reflectivity requires the presence of a fault zone of finite thickness with lower impedance material (e.g., associated with fault gouge, alteration minerals, and/or elevated pore fluid pressures) embedded within higher impedance country rock [*Bangs and Westbrook*, 1991; *Tobin et al*., 1994; *Ranero et al*., 2003].

From the upper mantle reflectivity along the Oregon transect, an estimate of the extent of shallow mantle hydration near the deformation front can be obtained. The absence of resolvable top and bottom reflections indicates that fault zones must be thinner than the dominant seismic wavelength, and thin layers must exceed one eighth of the dominant seismic wavelength to be detected [*Widess*, 1973]. With the average dominant wavelength at shallow mantle being 600 m (dominant frequency 10–20 Hz, velocity 7.5–8.2 km/s), we infer that the mantle fault zones imaged by our data have widths of ~75–600 m (1/8 to ~1 average dominant wavelength). From the reflections beneath Moho observed within 40 km from the deformation front, we estimate a combined fault length of ~30 km and a cumulative fault zone volume of ~1–8% of the upper 6 km of mantle in this region. Assuming the imaged fault zones are fully serpentinized with 13 wt % water [*Faccenda*, 2014], the cumulative fault volume corresponds with chemically bound water equivalent to a column 0.023–0.18 km high per unit length of trench and 0.12–0.92 wt % water within the uppermost 6 km of the mantle. This estimate is only about 11–13% of the 0.17–1.7 km of water stored in the incoming plate mantle offshore Nicaragua estimated by *Ranero et al*. [2003] and is consistent with predictions of more limited plate hydration at Cascadia due to the younger age and warm thermal state of the JdF plate.

It is intriguing that fault plane reflectivity in the crust and mantle is not always observed where bending-related faulting and alteration is documented along the global subduction system. For example, at the Kuril trench, Japan trench, and Alaska subduction zone there is compelling evidence for extensive bending-related faulting from seafloor bathymetry and for significantly reduced crustal and mantle velocities in the downgoing plate, but reflections off fault planes within the crust and mantle are not detected [e.g., *Tsuru et al*., 2000; *Fujie et al*., 2013; *Shillington et al*., 2015]. To date, pervasive bending fault reflections in the crust and mantle have only been reported at the Middle America trench offshore Nicaragua [*Ranero et al*., 2003]. Although there is extensive MCS coverage along the southern Chile margin where bend faulting is documented, only one reflective crustal/mantle fault at 39°S, 50 km from the deformation front, has been reported [*Grevemeyer et al*., 2005]. Why bend faults are seismically reflective at only some margins is unclear. Imaging limitations associated with data acquisition and processing may provide one possible explanation. However, the recent Kuril trench and Alaska studies used a similar data acquisition configuration as in our study, as well as advanced processing techniques, yet no reflective crustal/mantle faults are imaged. We note that at all locations where reflective crustal and mantle faults have been imaged (Cascadia, Nicaragua, and Chile), the downgoing plate is relatively young and warm. Under these conditions, circulating fluids in the crust may be warmer and more reactive, contributing to enhanced fault zone alteration and the observed crustal and mantle reflectivity.

At Cascadia, the incoming JdF plate is buried at young crustal ages by a low-permeability sediment blanket, which limits direct seawater exchange between the ocean and the igneous crust [e.g., *Davis et al*., 1999]. Although faults are present within the sediments, estimated fault growth rates are far less than sedimentation rates in this region [*Nedimović et al*., 2009], and open pathways for seawater to flow through the sediments and along deep-penetrating crustal faults are unlikely to exist for significant time periods. What then is the source of the fluids needed to generate the extensive fault zone alteration inferred within the bend fault region? One possible source is fluids residing in the porous upper crust. As bending-related deformation progresses, fracturing is enhanced and porosity will increase within crustal fault zones. Pressure gradients associated with this deformation may drive downward pore fluid flow [*Mancktelow*, 2008; *Faccenda et al*., 2009], leading to a larger fluid flux and greater hydrothermal alteration along fault planes. Second, close to the deformation front, as temperatures and pressures within the lower sediment section increase, the release of water through compaction and clay mineral dehydration (mainly smectite to illite transition) may be significant [*Saffer and Tobin*, 2011]. As estimated basement temperatures within a few tens of kilometers from the deformation front are ~106–170°C in our study region [*Moran and Lister*, 1987; *Johnson et al*., 2012], the smectite to illite transition, which occurs over temperatures of 60–160°C [*Bekins et al*., 1994], is likely to take place in the lower sediment section seaward of the deformation front [*Saffer et al*., 2008]. The sediment-derived water, which is warm, may enhance alteration reactions within fault zones, thus contributing to the increased seismic reflectivity.

5.4. Origin of Lower Crustal Ridgeward Dipping Reflectors

High-amplitude LCRs that extend downward from ~1000 to 1100 ms beneath the basement, dip consistently toward the mid-ocean ridge, and merge into Moho reflections at an angle of ~20–40° are imaged in 6–8 Ma old crust along both our Oregon and Washington transects (Figures 2, 3, 5, and 7). Where these reflections are observed, the crust is characterized by a relatively smooth basement topography and a highly reflective Moho. Although the upper crust above these events is densely faulted as indicated by small offsets at the basement and the presence of faint fault plane reflectivity in the upper crust, the ridgeward dipping LCRs do not connect to these basement offsets or upper crustal reflections. Rather, they appear to initiate at or below subhorizontal reflections in the midcrust, extend through the lower crust at low dip angles, and terminate at the Moho with no evidence for offsets of the Moho reflection. Based on these characteristics, it is unlikely that these LCRs arise from brittle fault zones in the lower crust.

LCRs with very similar characteristics have been reported in old oceanic crust generated at fast to superfast spreading ridges including Cretateous age crust in the NW Pacific off Japan [*Ranero et al*., 1997b; *Reston et al*., 1999; *Kodaira et al*., 2014], in 53–55 Ma old crust offshore Alaska [*Bécel et al*., 2015], in ~15 Ma old crust in the middle of the Cocos Plate [*Hallenborg et al*., 2003], and in ~0–85 Ma old crust east of Hawaii [*Eittreim et al*., 1994]. Oceanic crust generated at slow-spreading ridges is generally more reflective with many reflective events interpreted as being of tectonic origin [e.g., *Mutter and Karson*, 1992; *Ranero et al*., 1997a], but there are examples [e.g., *McCarthy et al*., 1988] that are strikingly similar to the LCRs seen in fast-spreading Pacific oceanic crust. Two primary hypotheses have been proposed for the origin of these ridgeward dipping LCRs [*Ranero et al*., 1997b; *Reston et al*., 1999]. The first is that they arise from lithological layering resulting from the downward and outward flow of material within mid-ocean ridge magma chambers during crustal formation [e.g., *Henstock et al*., 1993; *Phipps Morgan and Chen*, 1993]. The second hypothesis is that these LCRs represent ductile shear zones formed in the crust near the ridge by subcrustal basal drag when the uppermost mantle flow exceeds the rate of crustal formation, which may occur under conditions of active mantle upwelling [*Reston et al*., 1999]. *Ranero et al*. [1997b] and *Reston et al*. [1999] favored the lithological layering hypothesis, as the LCRs they imaged do not appear to display the upward flattening predicted by the shear zone hypothesis. However, this hypothesis does not readily account for the discrete spacing of the LCRs but rather predicts a pervasive fabric in the lower crust. The recent observations of *Kodaira et al*. [2014] provide renewed support for the shear zone hypothesis. In a region where ridgeward dipping LCRs are imaged, *Kodaira et al*. [2014] observe anomalously large seismic anisotropy in the uppermost mantle, which they attribute to faster mantle flow with respect to plate motion during crustal formation. They propose that the dipping reflections in the lower crust are shear zones formed near the ridge in response to basal drag forces associated with the faster flowing underlying mantle.

Our observations provide new constraints on the origin of these distinctive reflections in that (1) the presence of LCR events in same age crust in regions located 300 km apart provides strong evidence that these features reflect accretionary processes at the JdFR and (2) that these events are only observed in 6–8 Ma old crust and not in crust of older or younger ages, suggests that LCR formation is associated with anomalous accretionary processes during this time period.

Temporal variations in accretionary processes at the JdFR could be linked to the Cobb hotspot and its changing proximity to the ridge axis through time. The Cobb hotspot, which is currently located beneath or close to Axial Volcano, is a stationary melt anomaly possibly confined to the upper mantle as it is devoid of the isotopic characteristics typically associated with deep mantle plumes [*Desonie and Duncan*, 1990; *Chadwick et al*., 2005]. During the period of LCR formation (6–8 Ma), the Cobb hotspot was located 90–130 km from the ridge axis [*Desonie and Duncan*, 1990; *Karsten and Delaney*, 1989], likely too far for this melt anomaly to significantly influence the ridge axis-centered melting zone [*Ito et al*., 2003]. Furthermore, as the JdFR has migrated to the northwest toward the hotspot, the influence of Cobb on the ridge axis melting regime is expected to have progressively increased with decreasing crustal age, yet LCRs are only observed for the 6–8 Ma time period.

Temporal variations in accretionary processes could also be linked to the well-documented changes in the motion of the JdF plate over the past 40 Ma, which include two ~10° clockwise rotations relative to North America that occurred at ~5.89 and 8.5 Ma [*Wilson et al*., 1984; *Wilson*, 1988, 1993]. These two plate rotation events bound the time period of LCR formation. Spreading rates remained close to uniform throughout these plate reorganizations and well within the intermediate rate range (half spreading rates calculated from *Wilson*

[1993] for the past 9 Ma are 27.5–29.0 mm/yr and 26.6–29.4 mm/yr at the current latitudes of Endeavour Ridge and Axial Volcano, respectively). The time period of LCR formation also roughly correlates with a regional late Miocene unconformity (6–7.5 Ma), which is widely observed in the forearc basins of central Cascadia [*McNeill et al*., 2000]. *McNeill et al*. [2000] propose that this unconformity was formed by tectonic uplift resulting from the rotation of the Pacific and JdF plates relative to the North America plate and possible eustatic sea level fall that resulted in global hiatus NH6. We speculate that these plate reorganization events were associated with periods of anomalous mantle melting or less efficient mantle melt delivery at the mid-ocean ridge with the subridge asthenosphere moving faster than the crust, thus giving rise to shear in the ductile lower crust and forming the LCRs as proposed by *Kodaira et al*. [2014]. As reviewed by *Bécel et al*. [2015], in other regions where LCRs are found, such as the oceanic crust offshore Alaska [*Bécel et al*., 2015] and NW Pacific crust [*Kodaira et al*., 2014; *Ranero et al*., 1997b], plate reorganization associated with ridge jumps or rift propagation is also documented, although this hypothesis does not explain the nearly continuous observation of LCRs from 0 to 85 Ma in central Pacific crust [*Eittreim et al*., 1994].

Although our observations are consistent with LCRs forming near the spreading center as a result of temporal variation in mantle melt delivery, it is possible that the seismic reflectivity of these events is later enhanced by hydrothermal alteration [*Hallenborg et al*., 2003]. The upper crust above these LCRs is densely faulted, and we observe fault plane reflections reaching close to the LCRs at a few locations. We speculate that water percolating through these faults may reach the lower crust and become channelized along the LCR as local zones of heterogeneity, leading to enhanced alteration, which may help illuminate these events.

6. Summary

From the PSTM images along the 390 km long and 220 km long crossplate transects from the JdFR to the Cascadia deformation front offshore Oregon and Washington, we characterize for the first time the structure of the sediment, oceanic crust, and shallow mantle of the JdF Plate from zero age to 8–9 Ma prior to subduction and document in detail the distribution and extent of faulting within this plate. Our primary findings are summarized below:

1. Within the plate interior our images reveal numerous small offset faults in the sediment section beginning 50–70 km from the ridge axis, confirming previous inferences of a broad zone of faulting across the Juan de Fuca plate [*Nedimović et al*., 2009]. Fault offset shows little growth across the plate interior until near the deformation front. Beneath the sediment blanket, sparse dipping reflections from presumed hydrated abyssal hill faults are observed. These faults are largely confined to the upper crust, which is consistent with the inferred depth extent of abyssal hill faulting at intermediate-spreading ridges.
2. From basement topography, we infer that the JdF plate begins to deflect due to sediment loading at ~145–150 km and 120–125 km seaward from the deformation front on the Oregon and Washington transects and due to the combined effect of sediment loading and subduction at ~75–80 km and 65–70 km seaward from the deformation front. Bend faulting deformation is largely focused within 40 km from the deformation front in both regions with increases in sediment fault offsets and development of fault plane reflectivity in the crust and, on the Oregon transect, into the mantle.
3. The bright fault plane reflections observed on the Oregon transect that extend through the crust and 6–7 km into the mantle are similar to those previously imaged offshore Nicaragua by *Ranero et al*. [2003] and attributed to hydrated fault zones due to subduction bend faulting. Assuming serpentinization along the fault zones, we estimate ~ 0.12–0.92 wt % hydration of the uppermost 6 km of the mantle in this region, which is ~11–13% of the estimated water contained in the incoming plate mantle offshore Nicaragua [*Ranero et al*., 2003]. On the Washington transect, subduction bending faults are confined to the sediment section and upper-middle crust and more limited plate hydration in this region is inferred.
4. In other subduction zones, intermediate-depth intraslab earthquakes have been linked to plate hydration due to subduction bend faulting along the outer trench slope [e.g., *Ranero et al*., 2005; *Shillington et al*., 2015]. While limited bend faulting and inferred plate hydration at Cascadia is consistent with sparse intraslab seismicity at this subduction zone, the regional distribution of the seismicity that is detected cannot be readily attributed to only bend faulting-related hydration. Intraslab stresses associated with slab warping [*Crosson and Owens*, 1987; *McCrory et al*., 2012] or variation in mantle resistance [*Wada et al*., 2010] may be the dominant mechanism contributing to the occurrence of intermediate-depth intraslab earthquakes at Cascadia.

5. A series of distinct ridgeward dipping (dips 20–40°) reflections are imaged in same age (6–8 Ma) crust in the plate interior along the Oregon transect and near the deformation front along the Washington transect. These structures are very similar to lower crustal reflectors observed elsewhere in the Pacific and Atlantic. We interpret these features as ductile shear zones in the lower crust formed due to temporal variations in mantle upwelling associated with plate reorganizations at 8.5 and 5.9 Ma.

Acknowledgments
We thank the *R/V M.G. Langseth*'s Captain M. Landow, crew, and technical staff led by R. Steinhaus for their efforts, which made possible the success of cruise MGL1211. Seismic data processing and interpretation was conducted using the Paradigm processing software packages Focus, Geodepth, and VoxelGeo. All MCS field data, seismic navigation, and acquisition logs are archived with the IEDA: Marine Geoscience Data System (doi: 10.1594/IEDA/319000). The processed seismic data are archived at Academic Seismic Portal (doi: 10.1594/IEDA/500069). We thank two anonymous reviewers for insightful comments and suggestions, which greatly improved the paper. This research was supported by NSF grant OCE 1029411 to S.M.C., H.C., and M.R.N. and 1029305 to J.P.C.

References

Abers, G. A., L. S. MacKenzie, S. Rondenay, Z. Zhang, A. G. Wech, and K. C. Creager (2009), Imaging the source region of Cascadia tremor and intermediate-depth earthquakes, *Geology*, *37*(12), 1119–1122, doi:10.1130/g30143a.1.

Abers, G. A., J. Nakajima, P. E. van Keken, S. Kita, and B. R. Hacker (2013), Thermal-petrological controls on the location of earthquakes within subducting plates, *Earth Planet. Sci. Lett.*, *369*, 178–187, doi:10.1016/j.epsl.2013.03.022.

Adam, C., V. Vidal, and A. Bonneville (2005), MiFil: A method to characterize seafloor swells with application to the south central Pacific, *Geochem. Geophys. Geosyst.*, *6*, Q01003, doi:10.1029/2004GC000814.

Adam, J., D. Klaeschen, N. Kukowski, and E. Flueh (2004), Upward delamination of Cascadia Basin sediment infill with landward frontal accretion thrusting caused by rapid glacial age material flux, *Tectonics*, *23*, TC3009, doi:10.1029/2002TC001475.

Aghaei, O., M. R. Nedimović, H. Carton, S. M. Carbotte, J. P. Canales, and J. C. Mutter (2014), Crustal thickness and Moho character of the fast-spreading East Pacific Rise from 9 degrees 42′N to 9 degrees 57′N from poststack-migrated 3-D MCS data, *Geochem. Geophys. Geosyst.*, *15*, 634–657, doi:10.1002/2013GC005069.

Arnulf, A. F., A. J. Harding, G. M. Kent, S. M. Carbotte, J. P. Canales, and M. R. Nedimović (2014), Anatomy of an active submarine volcano, *Geology*, *42*(8), 655–658, doi:10.1130/g35629.1.

Atwater, B. F., and E. Hemphill-Haley (1997), Recurrence intervals for great earthquakes of the past 3,500 years at northeastern Willapa Bay, Washington.

Audet, P., M. G. Bostock, N. I. Christensen, and S. M. Peacock (2009), Seismic evidence for overpressured subducted oceanic crust and sealing of the megathrust, *Nature*, *457*, 76–78.

Bangs, N. L. B., and G. K. Westbrook (1991), Seismic modeling of the decollement zone at the base of the Barbados ridge accretionary complex, *J. Geophys. Res.*, *96*(B3), 3853–3866, doi:10.1029/90JB02138.

Bangs, N. L. B., G. F. Moore, S. P. S. Gulick, E. M. Pangborn, H. J. Tobin, S. Kuramoto, and A. Taira (2009), Broad, weak regions of the Nankai Megathrust and implications for shallow coseismic slip, *Earth Planet. Sci. Lett.*, *284*(1–2), 44–49, doi:10.1016/j.epsl.2009.04.026.

Bangs, N. L., T. H. Shipley, S. P. S. Gulick, G. F. Moore, S. Kuromoto, and Y. Nakamura (2004), Evolution of the Nankai Trough decollement from the trench into the seismogenic zone: Inferences from three-dimensional seismic reflection imaging, *Geology*, *32*(4), 273–276, doi:10.1130/g20211.1.

Bécel, A., D. J. Shillington, M. R. Nedimović, S. C. Webb, and H. Kuehn (2015), Origin of dipping structures in fast-spreading oceanic lower crust offshore Alaska imaged by multichannel seismic data, *Earth Planet. Sci. Lett.*, *424*, 26–37.

Bekins, B., A. M. McCaffrey, and S. J. Dreiss (1994), Influence of kinetics on the smectite to illite transition in the Barbados accretionary prism, *J. Geophys. Res.*, *99*(B9), 18,147–18,158, doi:10.1029/94JB01187.

Bergman, E. A. (1986), Intraplate earthquakes and the state of stress in oceanic lithosphere, *Tectonophysics*, *132*(1), 1–35.

Billen, M., E. Cowgill, and E. Buer (2007), Determination of fault friction from reactivation of abyssal-hill faults in subduction zones, *Geology*, *35*(9), 819–822, doi:10.1130/g23847a.1.

Bohnenstiehl, D. R., and S. M. Carbotte (2001), Faulting patterns near 19 degrees 30′ S on the East Pacific Rise: Fault formation and growth at a superfast spreading center, *Geochem. Geophys. Geosyst.*, *2*(9), 1056, doi:10.1029/2001GC000156.

Booth-Rea, G., D. Klaeschen, I. Grevemeyer, and T. Reston (2008), Heterogeneous deformation in the Cascadia convergent margin and its relation to thermal gradient (Washington, NWUSA), *Tectonics*, *27*, TC4005, doi:10.1029/2007TC002209.

Bostock, M. G., R. D. Hyndman, S. Rondenay, and S. M. Peacock (2002), An inverted continental Moho and serpentinization of the forearc mantle, *Nature*, *417*(6888), 536–538, doi:10.1038/417536a.

Brocher, T. M., T. Parsons, A. M. Tréhu, C. M. Snelson, and M. A. Fisher (2003), Seismic evidence for widespread serpentinized forearc upper mantle along the Cascadia margin, *Geology*, *31*(3), 267–270.

Brudzinski, M. R., and R. M. Allen (2007), Segmentation in episodic tremor and slip all along Cascadia, *Geology*, *35*(10), 907–910, doi:10.1130/g23740a.1.

Canales, J. P., S. M. Carbotte, H. Carton, and M. R. Nedimović (2014), State of hydration of the Juan de Fuca plate along the Cascadia deformation front from controlled-source wide-angle seismic data, AGU Fall Meeting Abstracts, 1, 4615.

Carbotte, S. M., and K. C. Macdonald (1994), Comparison of sea-floor tectonic fabric at intermediate, fast, and super fast spreading ridges: Influence of spreading rate, plate motions, and ridge segmentation on fault patterns, *J. Geophys. Res.*, *99*(B7), 13,609–13,631, doi:10.1029/93JB02971.

Carbotte, S. M., M. R. Nedimović, J. P. Canales, G. M. Kent, A. J. Harding, and M. Marjanovic (2008), Variable crustal structure along the Juan de Fuca Ridge: Influence of on-axis hot spots and absolute plate motions, *Geochem. Geophys. Geosyst.*, *9*, Q08001, doi:10.1029/2007GC001922.

Carbotte, S. M., J. P. Canales, H. Carton, and M. R. Nedimović (2012a), Multi-channel seismic shot data from the Cascadia subduction zone acquired during the R/V Marcus Langseth expedition MGL1211 (2012) edited, Integrated Earth Data Applications (IEDA).

Carbotte, S. M., J. Canales, H. D. Carton, M. R. Nedimović, S. Han, M. Marjanovic, J. C. Gibson, H. A. Janiszewski, G. Horning, and M. Delescluse (2012b), Evolution and hydration of the Juan de Fuca crust and uppermost mantle: A plate-scale seismic investigation from ridge to trench, AGU Fall Meeting Abstracts, 1, 01.

Carton, H., J. P. Canales, S. Janiszewski, S. M. Carbotte, G. Abers, A. Trehu, and M. R. Nedimović (2013), Structure of the Juan de Fuca plate and Washington forearc from 2D travel time tomography of OBS and land seismometer data along an east-west transect, AGU Fall Meeting Abstract, 1.2444.

Chadwick, J., M. Perfit, I. Ridley, I. Jonasson, G. Kamenov, W. Chadwick, R. Embley, P. Le Roux, and M. Smith (2005), Magmatic effects of the Cobb hot spot on the Juan de Fuca Ridge, *J. Geophys. Res.*, *110*, B03101, doi:10.1029/2003JB002767.

Choo, J., J. Downton, and J. Dewar (2004), Lift: A new and practical approach to noise and multiple attenuation, *First Break*, *22*(5), 39–44.

Contreras-Reyes, E., and A. Osses (2010), Lithospheric flexure modelling seaward of the Chile trench: Implications for oceanic plate weakening in the Trench Outer Rise region, *Geophys. J. Int.*, *182*(1), 97–112, doi:10.1111/j.1365-246X.2010.04629.x.

Contreras-Reyes, E., I. Grevemeyer, A. B. Watts, E. R. Flueh, C. Peirce, S. Moeller, and C. Papenberg (2011), Deep seismic structure of the Tonga subduction zone: Implications for mantle hydration, tectonic erosion, and arc magmatism, *J. Geophys. Res.*, *116*, B10103, doi:10.1029/2011JB008434.

Cordsen, A., M. Galbraith, and J. Peirce (2000), *Planning Land 3-D Seismic Surveys*, Soc. of Explor. Geophys., Tulsa, Okla.

Creager, K. C., L. A. Preston, R. S. Crosson, T. Van Wagoner, A. M. Tréhu, and S. H. I. P. S. W. Group (2002), Three-dimensional reflection image of the subducting Juan de Fuca plate, *The Cascadia Subduction Zone and Related Subduction Systems—Seismic Structure, Intraslab Earthquakes and Processes, and Earthquake Hazards*, *2*, 37.

Crosson, R. S., and T. J. Owens (1987), Slab geometry of the cascadia subduction zone beneath Washington from earthquake hypocenters and teleseismic converted waves, *Geophys. Res. Lett.*, *14*(8), 824–827, doi:10.1029/GL014i008p00824.

Davis, E. E., and R. D. Hyndman (1989), Accretion and recent deformation of sediments along the northern Cascadia subduction zone, *Geol. Soc. Am. Bull.*, *101*(11), 1465–1480.

Davis, E. E., D. S. Chapman, K. Wang, H. Villinger, A. T. Fisher, S. W. Robinson, J. Grigel, D. Pribnow, J. Stein, and K. Becker (1999), Regional heat flow variations across the sedimented Juan de Fuca Ridge eastern flank: Constraints on lithospheric cooling and lateral hydrothermal heat transport, *J. Geophys. Res.*, *104*(17), 675–688.

DeMets, C., R. G. Gordon, and D. F. Argus (2010), Geologically current plate motions, *Geophys. J. Int.*, *181*(1), 1–80.

Desonie, D. L., and R. A. Duncan (1990), The Cobb-Eickelberg seamount chain: Hotspot volcanism with midocean ridge basalt affinity, *J. Geophys. Res.*, *95*(B8), 12,697–12,711, doi:10.1029/JB095iB08p12697.

Eittreim, S. L., H. Gnibidenko, C. E. Helsley, R. Sliter, D. Mann, and N. Ragozin (1994), Oceanic crustal thickness and seismic character along a central Pacific transect, *J. Geophys. Res.*, *99*(B2), 3139–3145, doi:10.1029/93JB02967.

Faccenda, M. (2014), Water in the slab: A trilogy, *Tectonophysics*, *614*, 1–30.

Faccenda, M., T. V. Gerya, and L. Burlini (2009), Deep slab hydration induced by bending-related variations in tectonic pressure, *Nat. Geosci.*, *2*(11), 790–793, doi:10.1038/ngeo656.

Fisher, A. T., et al. (2003), Hydrothermal recharge and dischargeacross 50 km guided by seamounts on a young ridge flank, *Nature*, *421*, 618–621, doi:10.1038/nature01352.

Flueh, E. R., et al. (1998), New seismic images of the Cascadia subduction zone from cruise SO108-ORWELL, *Tectonophysics*, *293*(1–2), 69–84, doi:10.1016/s0040-1951(98)00091-2.

Fujie, G., S. Kodaira, M. Yamashita, T. Sato, T. Takahashi, and N. Takahashi (2013), Systematic changes in the incoming plate structure at the Kuril trench, *Geophys. Res. Lett.*, *40*, 88–93, doi:10.1029/2012gl054340.

Gerdom, M., A. M. Trehu, E. R. Flueh, and D. Klaeschen (2000), The continental margin off Oregon from seismic investigations, *Tectonophysics*, *329*(1–4), 79–97, doi:10.1016/s0040-1951(00)00190-6.

Gibson, J. C., S. M. Carbotte, S. Han, M. R. Nedimović, J. P. Canales, and H. D. Carton (2014), Analysis of faulting and sediment velocity characteristics outboard of the cascadia deformation front from multi-channel seismic data, AGU Fall Meeting Abstracts, *1*, 4614.

Goldfinger, C., C. H. Nelson, and J. E. Johnson (2003), Holocene earthquake records from the Cascadia subduction zone and northern San Andreas fault based on precise dating of offshore turbidites, *Annu. Rev. Earth Planet. Sci.*, *31*(1), 555–577.

Grevemeyer, I., and W. Weigel (1996), Seismic velocities of the uppermost igneous crust versus age, *Geophys. J. Int.*, *124*, 631–635.

Grevemeyer, I., N. Kaul, J. L. Diaz-Naveas, H. W. Villinger, C. R. Ranero, and C. Reichert (2005), Heat flow and bending-related faulting at subduction trenches: Case studies offshore of Nicaragua and Central Chile, *Earth Planet. Sci. Lett.*, *236*(1–2), 238–248, doi:10.1016/j.epsl.2005.04.048.

Hacker, B. R., S. M. Peacock, G. A. Abers, and S. D. Holloway (2003), Subduction factory: 2. Are intermediate-depth earthquakes in subducting slabs linked to metamorphic dehydration reactions?, *J. Geophys. Res.*, *108*(B1), 2030, doi:10.1029/2001JB001129.

Hallenborg, E., A. J. Harding, G. M. Kent (2003), Seismic structure of 15 Ma oceanic crust formed at an ultrafast spreading East Pacific Rise: Evidence for kilometer-scale fracturing from dipping reflectors, *J. Geophys. Res.*, *108*(B11), 2532, doi:10.1029/2003JB002400.

Han, S. (2015) "Accretion and subduction of oceanic lithosphere: 2D and 3D seismic studies of off-axis magma lenses at East Pacific Rise 9° 37–40'N area and downgoing Juan de Fuca Plate at Cascadia Subduction Zone", PhD thesis, Columbia Univ.

Han, S., S. M. Carbotte, H. D. Carton, J. Canales, and M. R. Nedimovic (2013), Multichannel seismic images of Cascadia Forearc structure at the Oregon Margin, AGU Fall Meeting Abstracts, 1. 2440.

Hayman, N. W., and J. A. Karson (2009), Crustal faults exposed in the Pito Deep Rift: Conduits for hydrothermal fluids on the southeast Pacific Rise, *Geochem. Geophys. Geosyst.*, *10*, Q02013, doi:10.1029/2008GC002319.

Henstock, T. J., A. W. Woods, and R. S. White (1993), The accretion of oceanic-crust by episodic sill intrusion, *J. Geophys. Res.*, *98*(B3), 4143–4161, doi:10.1029/92JB02661.

Hey, R. (1977), A new class of "pseudofaults" and their bearing on plate tectonics: A propagating rift model, *Earth Planet. Sci. Lett.*, *37*(2), 321–325.

Horning, G., J. P. Canales, S. M. Carbotte, M. R. Nedimović, and H. D. Carton (2014), Crustal structure and evolution of the southern Juan de Fuca plate from wide-angle seismic data: Insights into the hydration state of the incoming plate off Cascadia subduction zone, AGU Fall Meeting Abstracts, 1, 4616.

Hyndman, R. D. (1988), Deep seismic reflectors, electrically conductive zones, and trapped water in the crust over a subducting plate, *J. Geophys. Res.*, *93*(11), 13,391–13,405, doi:10.1029/JB093iB11p13391.

Hyndman, R. D. (2007), The seismogenic zone of subduction thrust faults: What we know and don't know, in *The Seismogenic Zone of Subduction Thrust Faults*, edited by T. H. Dixon and J. C. Moore, pp. 15–40, Columbia Univ. Press, New York.

Hyndman, R. D., and K. Wang (1995), The rupture zone of cascadia great earthquakes from current deformation and the thermal regime, *J. Geophys. Res.*, *100*(B11), 22,133–22,154, doi:10.1029/95JB01970.

Ito, G., J. Lin, and D. Graham (2003), Observational and theoretical studies of the dynamics of mantle plume-mid-ocean ridge interaction, *Rev. Geophys.*, *41*(4), 1017, doi:10.1029/2002RG000117.

Ivandic, M., I. Grevemeyer, A. Berhorst, E. R. Flueh, and K. McIntosh (2008), Impact of bending related faulting on the seismic properties of the incoming oceanic plate offshore of Nicaragua, *J. Geophys. Res.*, *113*(B5), B05410, doi:10.1029/2007JB005291.

Johnson, H. P., S. L. Hautala, and T. A. Bjorklund (2012), The thermal environment of Cascadia Basin, *Geochem. Geophys. Geosyst.*, *13*, Q07003, doi:10.1029/2011GC003922.

Kao, H., K. Wang, R.-Y. Chen, I. Wada, J. He, and S. D. Malone (2008), Identifying the rupture plane of the 2001 Nisqually, Washington, earthquake, *Bull. Seismol. Soc. Am.*, *98*(3), 1546–1558, doi:10.1785/0120070160.

Karsten, J. L., and J. R. Delaney (1989), Hot spot-ridge crest convergence in the northeast, Pacific, *J. Geophys. Res.*, *94*(B1), 700–712, doi:10.1029/JB094iB01p00700.

Kirby, S., R. E. Engdahl, and R. Denlinger (1996), Intermediate-depth intraslab earthquakes and arc volcanism as physical expressions of crustal and uppermost mantle metamorphism in subducting slabs, in *Subduction Top to Bottom*, vol. 96, pp. 195–214, AGU, Washington, D. C.

Kodaira, S., G. Fujie, M. Yamashita, T. Sato, T. Takahashi, and N. Takahashi (2014), Seismological evidence of mantle flow driving plate motions at a palaeo-spreading centre, *Nat. Geosci.*, *7*(5), 371–375, doi:10.1038/ngeo2121.

Lefeldt, M., I. Grevemeyer, J. Gossler, and J. Bialas (2009), Intraplate seismicity and related mantle hydration at the Nicaraguan trench outer rise, *Geophys. J. Int.*, *178*(2), 742–752, doi:10.1111/j.1365-246X.2009.04167.x.

Macdonald, K. C., P. J. Fox, R. T. Alexander, R. Pockalny, and P. Gente (1996), Volcanic growth faults and the origin of Pacific abyssal hills, *Nature*, *380*(6570), 125–129, doi:10.1038/380125a0.

MacKay, M. E. (1995), Structural variation and landward vergence at the toe of the Oregon accretionary prism, *Tectonics*, *14*(6), 1309–1320, doi:10.1029/95tc02320.

MacKay, M. E., G. F. Moore, G. R. Cochrane, J. C. Moore, and L. D. Kulm (1992), Landward vergence and oblique structural trends in the oregon margin accretionary prism: Implications and effect on fluid-flow, *Earth Planet. Sci. Lett.*, *109*(3–4), 477–491, doi:10.1016/0012-821x(92)90108-8.

Mancktelow, N. S. (2008), Tectonic pressure: Theoretical concepts and modelled examples, *Lithos*, *103*(1–2), 149–177, doi:10.1016/j.lithos.2007.09.013.

Masson, D. G. (1991), Fault patterns at outer trench walls, *Mar. Geophys. Res.*, *13*(3), 209–225, doi:10.1007/bf00369150.

McCarthy, J. I. L. L., J. C. Mutter, J. L. Morton, N. H. Sleep, and G. A. Thompson (1988), Relic magma chamber structures preserved within the Mesozoic North Atlantic crust?, *Geol. Soc. Am. Bull.*, *100*(9), 1423–1436.

McCrory, P. A., J. L. Blair, F. Waldhauser, and D. H. Oppenheimer (2012), Juan de Fuca slab geometry and its relation to Wadati-Benioff zone seismicity, *J. Geophys. Res.*, *117*(B9), B09306, doi:10.1029/2012JB009407.

McNeill, L. C., C. Goldfinger, L. D. Kulm, and R. S. Yeats (2000), Tectonics of the Neogene Cascadia forearc basin: Investigations of a deformed late Miocene unconformity, *Geol. Soc. Am. Bull.*, *112*(8), 1209–1224, doi:10.1130/0016-7606(2000)112<1209:totncf>2.3.co;2.

Moore, J. C., G. F. Moore, G. R. Cochrane, and H. J. Tobin (1995), Negative-polarity seismic reflections along faults of the Oregon accretionary prism: Indicators of overpressuring, *J. Geophys. Res.*, *100*(B7), 12,895–12,906, doi:10.1029/94JB02049.

Moran, J. E., and C. R. B. Lister (1987), Heat flow across Cascadia Basin near 47 N, 128 W, *J. Geophys. Res.*, *92*(B11), 11,416–11,432, doi:10.1029/JB092iB11p11416.

Mutter, J. C., and J. A. Karson (1992), Structural processes at slow-spreading ridges, *Science*, *257*(5070), 627–634, doi:10.1126/science.257.5070.627.

Nakanishi, M. (2011), Bending-related topographic structures of the subducting plate in the northwestern pacific ocean, in *Accretionary Prisms and Convergent Margin Tectonics in the Northwest Pacific Basin*, edited by Y. Ogawa, R. Anma, and Y. Dilek, pp. 1–38, Springer, Netherlands, doi:10.1007/978-90-481-8885-7_1.

Nedimović, M. R., R. D. Hyndman, K. Ramachandran, and G. D. Spence (2003), Reflection signature of seismic and aseismic slip on the northern Cascadia subduction interface, *Nature*, *424*(6947), 416–420, doi:10.1038/nature01840.

Nedimović, M. R., S. M. Carbotte, A. J. Harding, R. S. Detrick, J. P. Canales, J. B. Diebold, G. M. Kent, M. Tischer, and J. M. Babcock (2005), Frozen magma lenses below the oceanic crust, *Nature*, *436*(7054), 1149–1152, doi:10.1038/nature03944.

Nedimović, M. R., D. R. Bohnenstiehl, S. M. Carbotte, J. P. Canales, and R. P. Dziak (2009), Faulting and hydration of the Juan de Fuca plate system, *Earth Planet. Sci. Lett.*, *284*(1–2), 94–102, doi:10.1016/j.epsl.2009.04.013.

Parsons, T., A. M. Tréhu, J. A. Luetgert, K. Miller, F. Kilbride, R. E. Wells, M. Fisher, E. Flueh, U. ten Brink, and N. I. Christensen (1998), A new view into the Cascadia subduction zone and volcanic arc: Implications for earthquake hazards along the Washington margin, *Geology*, *26*, 199–202.

Phipps Morgan, J., and Y. J. Chen (1993), The genesis of oceanic-crust: Magma injection, hydrothermal circulation, and crustal flow, *J. Geophys. Res.*, *98*(B4), 6283–6297, doi:10.1029/92JB02650.

Plank, T., K. A. Kelley, M. M. Zimmer, E. H. Hauri, and P. J. Wallace (2013), Why do mafic arc magmas contain ~ 4 wt% water on average? *Earth Planet. Sci. Lett.*, *364*, 168–179.

Preston, L. A., K. C. Creager, R. S. Crosson, T. M. Brocher, and A. M. Trehu (2003), Intraslab earthquakes: Dehydration of the Cascadia slab, *Science*, *302*(5648), 1197–1200, doi:10.1126/science.1090751.

Ranero, C. R., E. Banda, and P. Buhl (1997a), The crustal structure of the Canary Basin: Accretion processes at slow spreading centers, *J. Geophys. Res.*, *102*(B5), 10,185–10,201, doi:10.1029/97JB00101.

Ranero, C. R., T. J. Reston, I. Belykh, and H. Gnibidenko (1997b), Reflective oceanic crust formed at a fast-spreading center in the Pacific, *Geology*, *25*(6), 499–502, doi:10.1130/0091-7613(1997)025<0499:rocfaa>2.3.co;2.

Ranero, C. R., J. P. Morgan, K. McIntosh, and C. Reichert (2003), Bending-related faulting and mantle serpentinization at the Middle America trench, *Nature*, *425*(6956), 367–373, doi:10.1038/nature01961.

Ranero, C. R., A. Villasenor, J. P. Morgan, and W. Weinrebe (2005), Relationship between bend-faulting at trenches and intermediate-depth seismicity, *Geochem. Geophys. Geosyst.*, *6*, Q12002, doi:10.1029/2005GC000997.

Reston, T. J., C. R. Ranero, and I. Belykh (1999), The structure of Cretaceous oceanic crust of the NW Pacific: Constraints on processes at fast spreading centers, *J. Geophys. Res.*, *104*(B1), 629–644, doi:10.1029/98JB02640.

Rogers, G. C., and R. S. Crosson (2002), Intraslab earthquakes beneath Georgia Strait/Puget Sound, *The Cascadia Subduction Zone and Related Subduction Systems—Seismic Structure, Intraslab Earthquakes and Processes, and Earthquake Hazards*, *2*, 65.

Rogers, G., and H. Dragert (2003), Episodic tremor and slip on the Cascadia subduction zone: The chatter of silent slip, *Science*, *300*, 1942.

Saffer, D. M., and H. J. Tobin (2011), Hydrogeology and mechanics of subduction zone forearcs: Fluid flow and pore pressure, *Annu. Rev. Earth Planet. Sci.*, *39*, 157–186.

Saffer, D. M., M. B. Underwood, and A. W. McKiernan (2008), Evaluation of factors controlling smectite transformation and fluid production in subduction zones: Application to the Nankai Trough, *Island Arc*, *17*(2), 208–230, doi:10.1111/j.1440-1738.2008.00614.x.

Shillington, D. J., A. Bécel, M. N. Nedimović, H. Kuehn, S. C. Webb, G. A. Abers, K. M. Keranen, J. Li, M. Delescluse, and G. A. Mattei-Salicrup (2015), Link between plate fabric, hydration and subduction zone seismicity in Alaska, *Nat. Geosci.*, *8*(12), 961–964, doi:10.1038/ngeo2586.

Smith, M. C., M. R. Perfit, and I. R. Jonasson (1994), Petrology and geochemistry of basalts from the southern Juan de Fuca ridge: Controls on the spatial and temporal evolution of midocean ridge basalt, *J. Geophys. Res.*, *99*(B3), 4787–4812, doi:10.1029/93JB02158.

Tilmann, F. J., I. Grevemeyer, E. R. Flueh, T. Dahm, and J. Gossler (2008), Seismicity in the outer rise offshore southern Chile: Indication of fluid effects in crust and mantle, *Earth Planet. Sci. Lett.*, *269*(1–2), 41–55, doi:10.1016/j.epsl.2008.01.044.

Tobin, H. J., J. C. Moore, and G. F. Moore (1994), Fluid pressure in the frontal thrust of the Oregon accretionary prism: Experimental constraints, *Geology*, *22*(11), 979–982, doi:10.1130/0091-7613(1994)022<0979:fpitft>2.3.co;2.

Tréhu, A. M., J. Braunmiller, and J. L. Nabelek (2008), Probable low-angle thrust earthquakes on the Juan de Fuca-North America plate boundary, *Geology*, *36*(2), 127–130, doi:10.1130/g24145a.1.

Tréhu, A. M., J. Braunmiller, and E. Davis (2015), Seismicity of the central Cascadia continental margin near 44.5° N: A decadal view, *Seismol. Res. Lett.*, *86*(3), doi:10.1785/0220140207.

Tsuru, T., J. O. Park, N. Takahashi, S. Kodaira, Y. Kido, Y. Kaneda, and Y. Kono (2000), Tectonic features of the Japan Trench convergent margin off Sanriku, northeastern Japan, revealed by multichannel seismic reflection data, *J. Geophys. Res.*, *105*(B7), 16,403–16,413, doi:10.1029/2000JB900132.

Turcotte, D. L., and G. Schubert (2002), *Geodynamics*, 456 pp., Cambridge Univ. Press, New York.

Underwood, M. B., K. D. Hoke, A. T. Fisher, E. E. Davis, E. Giambalvo, L. Zuhlsdorff, and G. A. Spinelli (2005), Provenance, stratigraphic architecture, and hydrogeologic influence of turbidites on the mid-ocean ridge flank of northwestern Cascadia Basin, Pacific Ocean, *J. Sediment. Res.*, *75*(1), 149–164, doi:10.2110/jsr.2005.012.

Van Avendonk, H. J. A., W. S. Holbrook, D. Lizarralde, and P. Denyer (2011), Structure and serpentinization of the subducting Cocos plate offshore Nicaragua and Costa Rica, *Geochem. Geophys. Geosyst.*, *12*, Q06009, doi:10.1029/2011GC003592.

Wada, I., S. Mazzotti, and K. Wang (2010), Intraslab stresses in the cascadia subduction zone from inversion of earthquake focal mechanisms, *Bull. Seismol. Soc. Am.*, *100*(5A), 2002–2013, doi:10.1785/0120090349.

Wang, K., J. H. He, and E. Davis (1997), Transform push, oblique subduction resistance, and intraplate stress of the Juan de Fuca plate, *J. Geophys. Res.*, *102*(B1), 661–674, doi:10.1029/96JB03114.

Watts, A. B. (2001), *Isostasy and Flexure of the Lithosphere*, Oxford Univ, Oxford, U. K.

Widess, M. B. (1973), How thin is a thin bed? *Geophysics*, *38*(6), 1176–1180.

Wiens, D. A., and S. Stein (1983), Age dependence of oceanic intraplate seismicity and implications for lithospheric evolution, *J. Geophys. Res.*, *88*(B8), 6455–6468, doi:10.1029/JB088iB08p06455.

Wilson, D. S. (1988), Tectonic history of the Juan de Fuca Ridge over the last 40 million years, *J. Geophys. Res.*, *93*(B10), 11,863–11,876, doi:10.1029/JB093iB10p11863.

Wilson, D. S. (1993), Confidence-intervals for motion and deformation of the Juan de Fuca plate, *J. Geophys. Res.*, *98*(B9), 16,053–16,071, doi:10.1029/93JB01227.

Wilson, D. S. (2002), The Juan de Fuca plate and slab: Isochron structure and Cenozoic plate motions, *Cascadia Subduction Zone Related Subduction Syst.*, *4350*, 9–12.

Wilson, D. S., R. N. Hey, and C. Nishimura (1984), Propagation as a mechanism of reorientation of the Juan de Fuca Ridge, *J. Geophys. Res.*, *89*(NB11), 9215–9225, doi:10.1029/JB089iB11p09215.